國立交通大學

光電工程研究所

博士論文

應用於照明系統之光度學量測與模擬方法

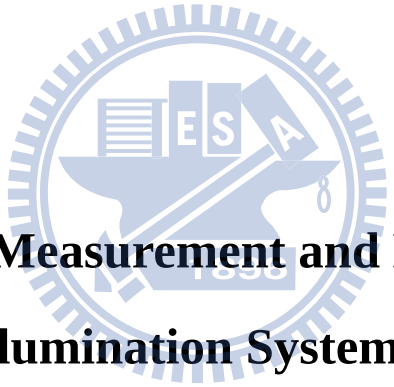

Photometric Measurement and Modeling for Illumination Systems

研究生：洪健翔

指導教授：田仲豪 副教授

中華民國九十九年七月

應用於照明系統之光度學量測與模擬方法

Photometric Measurement and Modeling for Illumination Systems

研 究 生: 洪健翔　　Student: Chien-Hsiang Hung
指導教授: 田仲豪　　Advisor: Prof. Chung-Hao Tien

國立交通大學
光電工程研究所

博士論文

A Thesis
Submitted to Institute of Electro-Optical Engineering
National Chiao-Tung University
in Partial Fulfillment of the Requirements
for the Degree of Doctor of Philosophy
In
Electro-Optical Engineering

July 2010
Hsin-Chu, Taiwan, Republic of China.

中華民國九十九年七月

應用於照明系統之光度學量測與模擬方法

研究生：洪健翔　　指導教授：田仲豪 副教授

國立交通大學
光電工程研究所

摘要

各式各樣的通訊產品與影音媒體不斷推陳出新，驅策著光電科技日新月異，而光學元件之需求量也與日俱增。隨著照明及顯示技術之開發，同時具有反射、折射、發光、及散射之複合功能的光電材料被大量使用(如:白光二極體之黃螢光粉層)，而其量測技術、光學模型、及計算方法需相應隨之進步，以配合系統開發者的需求。

本論文以幅度學及光度學理論為基礎，針對複合光學特性之光學材料提出新式的量測儀器、光學模型、以及計算方法，以各式光學材料做為驗證，並以提出之流程應用於新式平面光源系統開發。

首先，本論文以雙方向散射函數描述光學特性，結合錐光量測儀，建立一套雙方像散射函數之量測平台，成功測量出散射元件之光學特性，並對其雙方像散射函數做定性分析。其次，以白光二極體中螢光粉層為目標，提出雙色雙方向散射函數描述其光學特性，論文中敘述了其數學定義、實驗方法、及計算驗證。

除了提出新式雙方向函數模型，本論文亦針對此類雙方向模型對於光與物質交互作用之積分計算開發一套演算法。以有限取樣疊加代替積分，與參考光源比較，疊代找出目標物之最佳取樣密度，論文中敘述了其數學操作方法，並以計算商用光學擴散膜片做為演算法驗證。

以上述提出之新式量測技術、光學模型、以及計算方法，本論文對於一新型外加螢光膜片之平面光源做為應用，其平面光源系統之發光二極體陣列密度、空腔厚度皆以新式流程做光學模擬及特性預測，最終以優化參數成功實作出原形模組。

Photometric Measurement and Modeling for Illumination Systems

Student: Chien-Hsiang Hung **Advisor: Prof. Chung-Hao Tien**

Institute of Electro-Optical Engineering,
National Chiao Tung University

Abstract

Various communication and multimedia products are fast renewed, driving optoelectronics techniques to develop rapidly. As the progress of illumination and display technologies, multi-functional optoelectronics materials which simultaneously have the reflection, refraction, emission and scatter properties are commonly used (e.g. the yellow phosphor layer of white light emitting diodes). Thereby, the corresponding measurement technologies, optical modeling, and calculation methodologies should be developed for researchers.

In this dissertation, basing on the radiometry and photometry, we proposed a specific measurement instrument, optical characterization, and calculation method for these multi-functional optoelectronics materials. The experiments of some materials were implemented for verification. Furthermore, the proposed procedure was applied on the development of a novel planer lighting system with remote phosphor sheet.

Firstly, we used bidirectional scattering distribution function (BSDF) to describe the optical properties. A BSDF measurement instrument associated with a conoscopic system was created, and the properties of scattering components were measured. The BSDF data are also qualitatively analyzed. Most importantly, we proposed a dichromatic BSDF to characterize the optical properties of the yellow phosphor layer in a phosphor-converted LED. The mathematical definition, experimental method, and verification are stated in the thesis.

In addition to the dichromatic BSDF, an algorithm was proposed to calculate the energy integration of the light-material interaction characterized by such bidirectional models. A discrete superposition was applied to implement the integration. Comparing with a reference light source, the optimized discrete sampling grid of the target sample would be found by an iterative method. The mathematical operation process is introduced in this thesis, and the proposed algorithm was verified by a commercially available diffusing sheet.

By using the proposed measurement instrument, optical characterization, and

calculation method, a novel planer lighting system with remote phosphor sheet was simulated. The arrangements of LED array and cavity thickness were optimized through this procedure. Finally, the prototype module of the planer light source was demonstrated by the optimized geometrical parameters.

致謝

首先要感謝我指導教授田仲豪老師四年來在研究上、表達能力及生活細節上無私的細心指導，並且提供我們良好的研究環境，使我在博士生涯對於專業能力以及研究方法有深入的體悟，並順利完成本論文。

實驗室的日子裡，首先要感謝李企桓、方仁宇學長在研究上無私的指導與協助，還有鄭璧如學姊在研究過程提供許多寶貴的建議，跟我一起打仗的夥伴，簡銘進、陸彥行同學，我們互相鼓勵度過漫長的研究所生涯。同時還要感謝其他學長姊、同學和學弟在課業上、生活上、研究上的幫助與分享，並陪伴我一起度過四年快樂的日子。

另外，對於我的父親、母親、哥哥、及惠茹，我要感謝你們多年來的支持與鼓勵，還有生活上的細心照顧與關懷，使我能夠無後顧之憂的研究與學習，並順利完成博士學業。

最後，我要特別感謝寶文，四年前讓我有勇氣求取最高學歷，雖然過程中在各方面不斷遭遇挫折，但每在最艱難的時刻是妳給與我無形力量堅持下去，這成長的果實希望與妳一同分享。

Table of Contents

Figure Caption

Table Caption

Chapter 1

Introduction

1.1 Radiometry and Photometry

Radiation is the energy propagation by variable forms in space. The energy radiation exists due to the interaction of light sources, objects, and the human visual system. The relationships between the three components are illustrated in Fig. 1-1 [1]. In general, light sources are quantified by the spectral and spatial power distribution. Objects are specified by the transmitted, reflected, or scattered spectral distribution varied with the illuminating and viewing geometric relation. The human visual system is quantified through the color matching properties. Therefore, the quantification of energy propagation in the triangle can be characterized by radiometry and photometry.

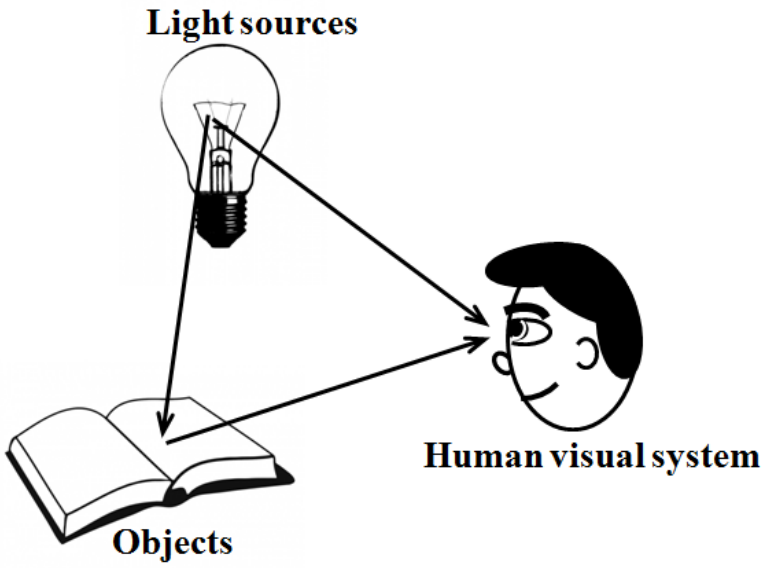

Fig. 1-1 the interaction of light sources, objects, and human visual system

1.1.1 Radiometric quantities

The subject of radiometry is a system of the terminology, mathematical relationships, measurement instruments, and units of light energy radiation, including the effects on that radiation of reflection, refraction, absorption, transmission, and scattering by material substances in their solid, liquid and gaseous phases [2]. This energy flow is concerned with the electromagnetic spectrum, illustrated in Fig. 1-2, which has labels for different portions of the spectrum of interest in different fields of study. The terminology shown in Table 1-1 was standardized by the International Commission on Illumination (CIE). The spectral range of visible radiation is the concerned portion for the lighting consideration.

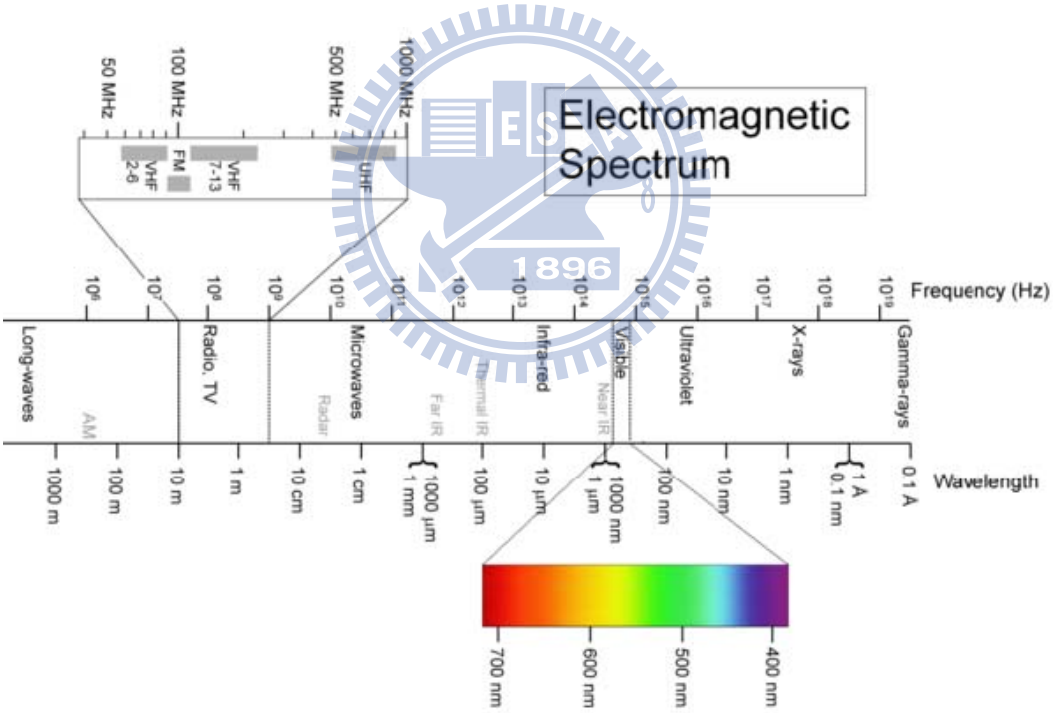

Fig. 1-2 Portions of the electromagnetic spectrum

Table 1-1 CIE vocabulary for spectral regions

Name	***Wavelength Range***
UV-C	100 to 280 nm
UV-B	280 to 315 nm
UV-A	315 to 400 nm
VIS	360-400 to 760-800 nm
IR-A	780 to 1400
IR-B	1.4 to 3 μm
IR-C	3 μm to 1 mm

The concepts of energy radiation are defined by geometrical optics, where rays propagate in a straight cone. Radiometric quantities include radiant energy, radiant flux, radiant intensity, irradiance, radiant exitance, and radiance. Table 1-2 shows these fundamental radiometric quantities whose unit is based on energy and SI units.

Table 1-2 Radiometric units.

Quantity	**Symbol**	**Definition**	**SI Units**
Radiant energy	Q_e	--	Joule
Radiant flux	Φ_e	dQ_e/dt	Watt
Radiant exitance	M_e	$d\Phi_e/dA$	$Watt/m^2$
Irradiance	E_e	$d\Phi_e/dA$	$Watt/m^2$
Radiant intensity	I_e	$d\Phi_e/d\Omega$	Watt/sr
Radiance	L_e	$dI_e/dA_\perp$	$Watt/sr \cdot m^2$

(t: time, Ω: solid angle, A: area)

Radiant energy Q defines the energy of a collection of photons (as in a laser plus). Radiant flux Φ is the energy flow per unit time. The power may be the total emitted from a source or the total landing on a particular surface. It's important to realize that the radiant flux is a function of position and direction. Basing on radiant flux Φ, the quantities of radiometry are derived by various geometric normalizations.

Projected area A

In the radiometric calculation, it's necessary to compute the foreshortened area as seen from a directional different from the surface normal. For example, if we look at a circular pattern from an oblique angle, it appears to be an elliptical shape with the apparent area smaller than the physical size. Fig. 1-3 shows the area *A* with a surface normal **N**. **V** is the viewing direction, and θ is the angle between **N** and **V**. Therefore, the area Aproj is the projected area of *A* in the direction of **V**. It is calculated as $A_{proj}=A\cos\theta$.

Solid angle

As a cone of rays radiating from a point source diverges at a rate proportional to the inverse of the square of the distance from the source, we must consider the spatial extent of the cone angle. The concept for this quantitative description is called the solid angle. The solid angle of a cone is defined as the area cut out by the cone on a unit sphere which is centered at the apex of the cone. If the intersection of a cone and the unit sphere has an area ω, we can define the cone has a solid angle ω. Thus, a sphere has a solid angle of 4π. If the intersection is between the cone and a sphere of radius r, the solid angle is equal to the intersection area divided by r^2.

Intensity *I*

Radiant intensity *I* is the quantity which describes the light output from a point source at the cone of unit solid angle. The definition of *I* is the radiant flux per unit solid angle,

$$I(x,y,z,\theta,\phi)=\frac{d\Phi(x,y,z,\theta,\phi)}{d\omega}\ \text{Wsr}^{-1}. \qquad (1.1)$$

It should be point out that light from a source of very small dimension has a very large coherent area. (see Fig. 1-4) At a distance very far away from the light source,

we can treat the light source as a point source. The point source is an idealization which has a spatial location but no physical dimension. Although there is no such thing as a point source, it is a useful approximation in practice. If the physical dimension of a source is one-tenth of the distance between the source and the object, the source can be treated as a point source and the error in the radiometric calculation is on the order of 10%.

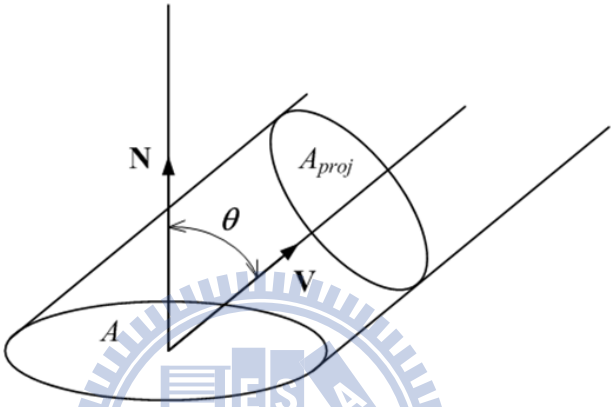

Fig. 1-3 The scheme of radiant intensity

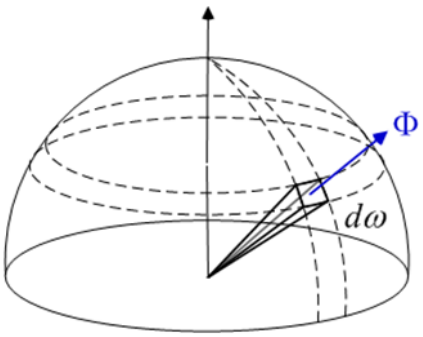

Fig. 1-4 The scheme of radiant intensity

Radiance *L*

If the light source is nearby, it can no longer be treated as a point source. The area of the source is divided into small elements d*A*, and each element can be treated as a

point source. However, because of the consideration of emitting area, the direction of the cone of rays is not perpendicular to the elemental surface. Here the projected area $dA\cos\theta$ should be used, where θ is the angle between the cone and the surface normal of the element. (see Fig. 1-5) The quantity that describes the amount of light coming from a surface is called the radiance, L, which is the light flux per solid angle per projected surface area,

$$L(x,y,z,\theta,\phi)=\frac{d\Phi(x,y,z,\theta,\phi)}{dA\cos\theta d\omega}\ \mathrm{Wsr^{-1}m^{-2}}. \tag{1.2}$$

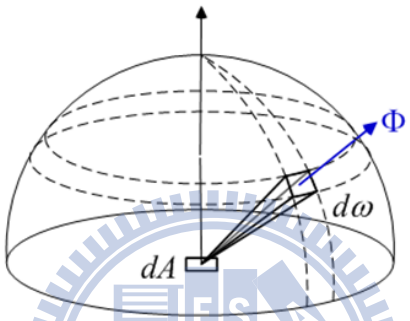

Fig. 1-5 The scheme of radiance

Irradiance *E* and radiant exitance *M*

Irradiance E and radiant exitance M describe how much light passes through a receiving and emitting surface, respectively. The definition is the radiant flux per unit area, as shown in Fig. 1-6 (a) and (b). In these definitions, E and M are functions of both position and direction.

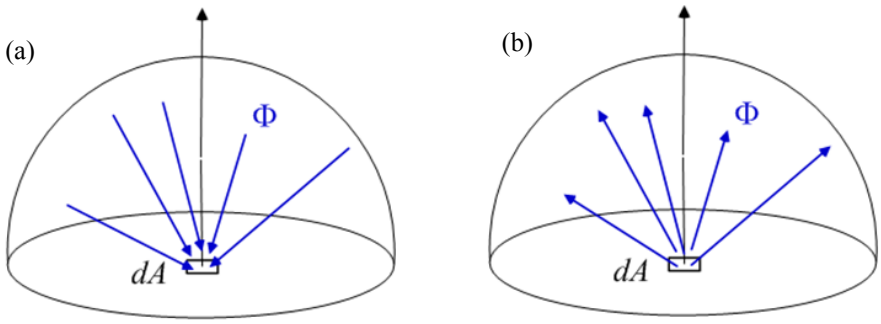

Fig. 1-6 The scheme of (a) irradiance E and (b) radiant exitance M

1.1.2 Photometric quantities

For human visual system, the responses to the optical radiation with different wavelengths are dissimilar. Photometric quantity is an operationally defined quantity designed to represent the way in which the human visual system evaluates the corresponding radiometric quantity. Accordingly, it is also called a psychophysical quantity. In particular, the optical radiation within the wavelengths range between 380 nm and 780 nm, so-called visible light, are discussed by photometry.

Photometric quantities include luminous energy, luminous flux, luminous intensity, illuminance, luminous exitance, and luminance. In geometric terms, the definitions of these photometric quantities are the same as for the corresponding radiometric quantities. Table.1-3 shows the photometric quantities whose unit is based on lumen (lm). Lumen is defined as 'luminous flux emitted into a solid angle of one steradian by a point source whose intensity is 1/60 of the intensity of 1 cm^2 of a blackbody at the temperature of platinum (2042K) under a pressure of one atmosphere.

From the definition of lumen, the maximum value of spectral luminous efficiency could be determined. At the wavelength 555 nm, which corresponds to the maximum spectral efficiency of human eyes, 1 watt is equal to 680 lumens. Therefore, the luminous flux Φ_v emitted by a source with a radiant flux Φ is given by:

$$\Phi_v = 683 \text{ lm/W} \cdot \int V(\lambda)\Phi(\lambda)d\lambda. \qquad (1.3)$$

where λ is the wavelength and $V(\lambda)$ is the spectral luminous efficiency function as shown in Fig.1-7.

Table 1-3 Photometric quantities.

Quantity	Symbol	Definition	SI Units
Luminous energy	Q_v	--	lumen • s
Luminous flux	Φ_v	dQ_v/dt	lumen (lm)
Luminous exitance	M_v	$d\Phi_v/dA$	lumen /m^2
Illuminance	E_v	$d\Phi_v/dA$	lumen /m^2 or lux
Luminous intensity	I_v	$d\Phi_v/d\Omega$	lumen /sr or candela
Luminance	L_v	$dI_v/dA_\perp$	lumen/sr • m^2 or nits

(t: time, Ω: solid angle, A: area)

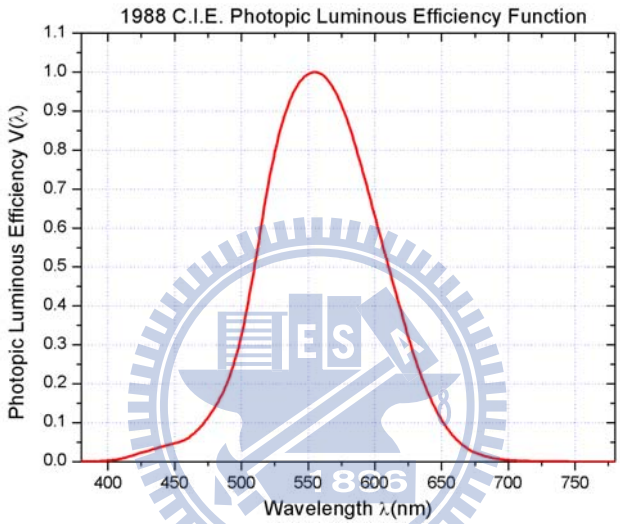

Fig. 1-7 Human visual response function.

1.1.3 Radiance theorem

In geometrical optics, light is treated as rays, and tracing rays from one point in space to another is an operation carried out in diverse applications. An implicit assumption in ray tracing is that each ray carries with energy flux through space. The radiometric quantity associated with each ray is called basic radiance which is defined as the radiance divided by the index of refraction squared. It can be proved that the basic radiance is conserved when light is propagated through non-absorbing and non-scattering material. This conservation property of the basic radiance is called the radiance theorem.

Fig. 1-8 shows the propagation of the basic radiance along a light ray through two different media. From Snell's law a ray with incident angle θ_1 is refracted to a transmission angle of θ_2,

$$n_1 \sin\theta_1 = n_2 \sin\theta_2. \tag{1.4}$$

Then, we take derivatives of both sides,

$$n_1 \cos\theta_1 d\theta_1 = n_2 \cos\theta_2 d\theta_2. \tag{1.5}$$

The radiant flux of the incident ray transmitted into the second medium is $d\Phi_1$, and the radiant flux of the transmitted ray in the second medium is $d\Phi_2$. We consider the conservation property $d\Phi_1 = d\Phi_2$, so

$$L_1 \cdot dA \cdot \cos\theta_1 \cdot \sin\theta_1 \cdot d\theta_1 \cdot d\phi_1 = L_2 \cdot dA \cdot \cos\theta_2 \cdot \sin\theta_2 \cdot d\theta_2 \cdot d\phi_2, \tag{1.6}$$

where f1=f2. From Eq. 1.4, 1.5, and 1.6, we have

$$\frac{L_1}{n_1^2} = \frac{L_2}{n_2^2} \tag{1.7}$$

Therefore, the basic radiance, L/n^2, is preserved. As we deal with spectral radiance, the radiant flux is measured per wavelength interval. The wavelength has to be scaled by n:

$$L_\lambda = dL/d\lambda = dL/(d\lambda_0/n), \tag{1.8}$$

and therefore,

$$dL/n^2 = L_\lambda \, d\lambda_0/n^3. \tag{1.9}$$

Since $dL_1/n_1^2 = dL_2/n_2^2$, we have

$$\frac{L_{\lambda_1}}{n_1^3} = \frac{L_{\lambda_2}}{n_2^3}. \tag{1.10}$$

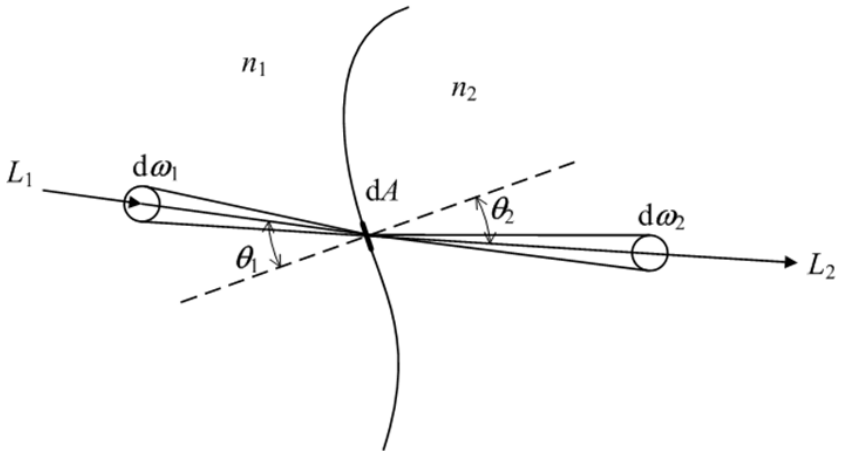

Fig. 1-8 The propagation of the basic radiance along a ray.

1.2 Energy Balance Equation

The radiometry of materials is the characterization of their interaction with light as illustrated in the lower left corner of the triangle in Fig. 1-1. In general, absorption, reflection, and transmission are the phenomena that take place when light interacts with the materials. Here the interaction process obeys the law of conservation of energy. The combined consideration of the absorbed, reflected and transmitted radiant flux must sum to the incident radiant energy at each wavelength. However, the interaction of radiant flux with objects is not a simple spectral phenomenon. In other words, the reflectance or transmittance of an object is not just a function of wavelength, but also a function of the illumination and viewing geometry. For instant, as the object in Fig. 1-1 is a reflective color display with a gloss surface. The glare caused from the ambient light would be observed with the colored information. It is usually classified into Lambertian, specular, and directional diffuse [3]. Surface properties affect the radiant power distribution versus the viewing direction. This is just one geometric appearance effect, which called physical scenes. To quantify such properties, the bidirectional scattering distribution function (BSDF) was defined for

each possible combination of illumination angle, viewing angle, and wavelength. The BSDF, which would be introduced in Chapter 2, is a function to connect the incoming radiant flux with the outgoing radiant energy. Therefore, the energy equilibrium for a set of radiating surfaces is expressed by the following integral equation [3]:

$$\underbrace{L(x,y,\omega_o,\lambda)}_{\text{total radiance}} = \underbrace{L_e(x,y,\omega_o,\lambda)}_{\text{emitted radiance}} + \underbrace{\int_\Omega \rho(x,y,\omega_i,\omega_o,\lambda)L_i(x,y,\omega_i,\lambda)\cos\theta d\omega_i}_{\text{scene physics}}. \quad (1.11)$$

$L(x, y, \omega_o, \lambda)$ is the radiance leaving point (x, y) in direction ω_o;

$L_e(x, y, \omega_o, \lambda)$ is the emitted radiance at point (x, y);

$L_i(x, y, \omega_i, \lambda)$ is the incident radiance impinging in point (x, y) from direction ω_i;

Ω is the set of direction ω_i in the hemisphere covering the surface at point (x, y);

$\rho(x, y, \omega_i, \omega_o, \lambda)$ is the bidirectional distribution function.

Eq. 1.11 describes the energy balance at point (x, y), as the outgoing radiance in terms of the various sources of radiant energy. The first term of the right-hand side is the emissivity of the surface. It is the case where the surface is a light source. The second term expresses the transformation process of physical scenes, such as reflection or transmission. The outgoing radiance is an integration over all possible incoming directions of the incoming irradiance times the bidirectional distribution function.

1.3 Motivation and Objectives

As the lighting technologies continuously progress, the classification between the light source and object in the triangle is gradually indeterminate. The emitted radiance and physical scenes should be both considered on some objects. For instant, as the object in Fig. 1-1 is the yttrium aluminum garnet (YAG) phosphor in a phosphor-converted light emitted diode (pcLED) (shown in Fig. 1-9) [4], which

scatters the illuminating flux and re-emits a fraction of the absorbed light at a different wavelength peak, measurement of the optical properties is prohibitively difficult, and produces massive quantities of data that are difficult to meaningfully utilize. The quantification indices characterizing the spectral and geometric relationship should be modified in an effective and a sensible way.

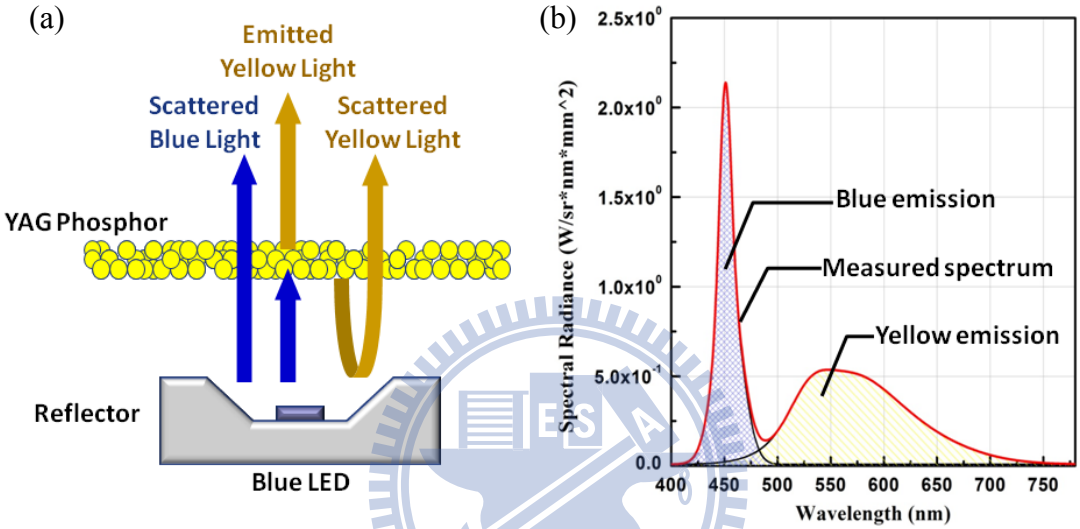

Fig. 1-9 YAG phosphor layer in a pcLED: (a) the schematic graph of the interaction; (b) the radiant spectral power distribution

Basing on the energy balance equation, the thesis attempts to study the measurement instruments, mathematical relationships, and calculation methodologies for illumination systems, such as luminaire and liquid crystal display (LCD) backlighting modules. First, the experimental setup for the bidirectional scattering distribution function (BSDF) measurement was developed [5]. Here the measurement instrument is associated with a conoscopic imaging system [6,7]. Next, a new mathematical definition, dichromatic BSDF, is introduced for the characterization of photo-fluorescent materials [8,9]. Here the YAG phosphor layer in a pcLED is introduced for demonstration. Then, a simple but effective calculation methodology

for the integration of the energy balance equation is described and demonstrated [10,11].

1.4 Organization

The rest of this thesis is organized as follows. In **Chapter 2**, for scene physics, the theory and operation principle of BSDF are introduced based on the photometry and radiometry. The BSDF measurement instrument was set up, and the measured bidirectional photometric data were analyzed. In **Chapter 3**, the proposed dichromatic BSDFs are introduced, and the YAG phosphor layer in a pcLED is considered as an example. After the BSDF, a calculation methodology of the integral equation, Eq. 1.6, is presented in **Chapter 4**. The concept was verified by the diffuser of a commercial available LCD backlighting module. In **Chapter 5**, by using the proposed methods, a novel planar lighting source by blue LEDs array with remote phosphor sheet was simulated as an application. Here the optical properties were predicted, and the geometric parameters were optimized for the demonstration of a 7-inch prototype. Finally, the conclusions of this thesis and recommendations for the future works are given in **Chapter 6**.

1.5 References

[1] Mark. D. Fairchild. *Color Appearance Models*, (John Wiley & Sons, Chichester, England, 2005).

[2] William. R. McCluney, *Introduction to Radiometry and Photometry*, (Artech House, Boston, 1994)

[3] Francois X. Sillion, and Claude Puech, *Radiosity and Global Illumination*, (Morgan Kaufmann Publishers Inc., San Francisco, 1994)

[4] R. Mueller-Mach, G. O. Mueller, M. R. Krames, and T. Trottier, "High-power phosphor-converted light-emitting diodes based on III-nitrides," IEEE J. Sel. Top. Quantum Electron. **8**, 339-345 (2002).

[5] John. C. Stover, *Optical Scattering: Measurement and Analysis*, (Mc Graw-Hill, New York, 1990).

[6] M. E. Becker, “Evaluation and characterization of display reflectance,” Displays **19**, 35-54 (1998).

[7] M. E. Becker, “Display Reflectance: Basics, Measurement, and Rating,” J. SID **14/11**, 1003-1017 (2006).

[8] C.-H. Hung, C.-H. Tien, “Phosphor-converted LED modeling by bidirectional photometric data,” Opt. Express (to be published).

[9] C.-H. Hung, C.-H. Tien, “Phosphor Modeling for Phosphor-converted LEDs,” SID Symposium Digest Tech., Papers 59.3, (2010).

[10] C.-H. Tien, and C.-H. Hung, “An iterative model of diffuse illumination from bidirectional photometric data,” Opt. Express **17**, 723-732 (2009).

[11] C.-H. Hung, C.-H. Tien, “Modeling Diffuse Components by Bidirectional Scatter Distribution Function for LCD Applications,” SID Symposium Digest Tech., Papers 36.4, (2009).

Chapter 2

Scene Physics

Light radiated from light sources is reflected, refracted, scattered, or diffracted by objects. As a result of all these light-matter interactions, light is redistributed spatially and temporally to create physical scenes that we can see. Thus, the study of illumination system should begin with the light-field formation process of physical scenes. This is what we mean by scene physics. BSDF is the most general expression of the light energy behavior passing through a surface or thin film. Although various materials in nature induce light in very different ways, which explains why their appearance can be dramatically different, the BSDFs can completely describe such optical phenomena. In this chapter, we first introduce the optical scattering, which is the basic of global illumination. Then, the BSDFs are defined basing on the radiometry. Finally, the BSDF measurement is presented and demonstrated.

2.1 Optical Scattering

To begin a discussion of scene physics, the light reflected by an object is considered. The optical properties of reflector materials can be specular, spread, or diffuse as shown in Fig. 2-1 [1]. Specular materials permit precise redirection of light rays and sharp cutoffs, while painted reflectors produce diffuse, scattered, or widespread light distribution. The high-reflectance materials with about 98% reflectivity can enhance lighting efficiency.

The scattered radiance distribution for an ideal diffuse surface is Lambertian. The distribution of scattered intensity is given by the following equation,

$$I(\theta) = I_0 \cdot \cos(\theta) \tag{2.1}$$

as illustrated in Fig. 2-2(a). The Gaussian distribution for a rough surface is shown in Fig. 2-2(b), and the distribution of scattered intensity varies according to the equation

$$I(\theta) = I_0 \cdot \exp[-\frac{1}{2}(\frac{\theta}{\sigma})^2], \tag{2.2}$$

where I_0 is the intensity in the specular direction, σ is the standard deviation of the Gaussian distribution.

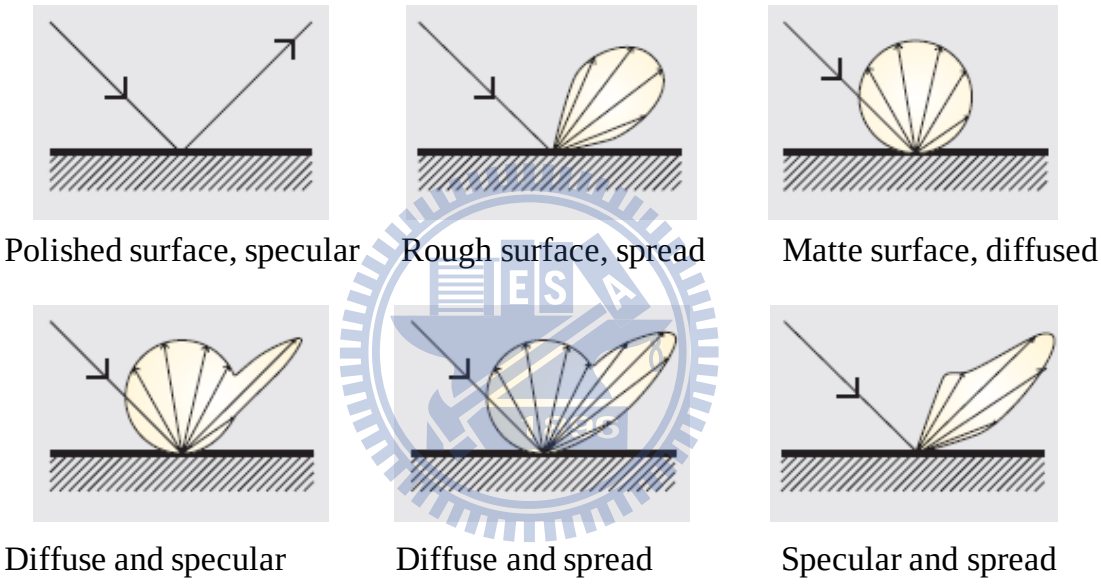

Fig. 2-1 Reflector materials and optical properties

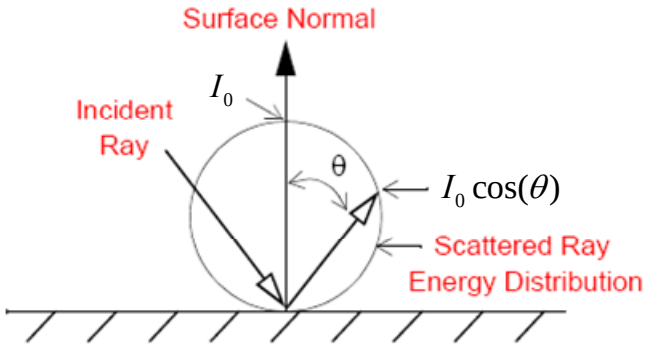

(a)

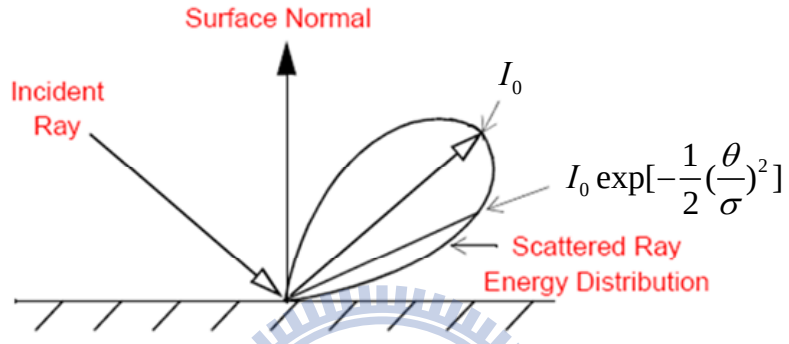

(b)

Fig. 2-2 (a) Lambertian distribution for a diffuse surface (b) Gaussian distribution for a rough surface

Scatter from transmission and reflection optics is mainly caused by several mechanisms including surface topography, surface contamination, bulk index fluctuations, and bulk particulates [2]. These scatter characteristics are introduced as the following.

Surface topography

By diffraction theory, surface topography induces phase deviations to the incident wavefront. In general, surface topography contributes multiple refractions and reflections on a ray. Thus, it's difficult to analyze the wavefront behavior through primary optics by the random surface vectors.

Surface contamination

The intensity and polarization of the scatter patterns by surface contamination

depend on particulate size, shape, and material constants. Particulates play a significant role in producing scatter.

Bulk index fluctuations

Index fluctuations induce a phase change to the transmitted beam through the film or the reflected beam by subsurface. As a diffraction effect, scatter from these flaws has a dependence on spot size similar to that of surface fluctuations.

Bulk particulates

Bulk particulate flaws are due to small bubbles, inclusions, and contamination. Bulk scatter caused by isolated particulates which are small compared to the wavelength is called Rayleigh scatter.

In general, rays scattered by a material behave as the combination of the four mechanisms. As Fig. 2-3 shows, we take rays scattered from a surface as example. As two light rays (r1 and r2) are incident on the surface between air and an object of some inhomogeneous material, part of their energy is reflected (r3 and r7) and part of it penetrates into the surface (r4 and r6). The reflected part may undergo many-times reflection (r7). The penetrating light may undergo multiple scattering by particles in the material, and then is absorbed (r6) or reflected back into the air (r5). This example shows the incident light may undergo the combination of the refraction, reflection, scattering, and absorption. The four material properties we mentioned may affect the incident light, simultaneously. Only in the ideal situation of a perfectly smooth surface of homogeneous material with infinite spatial extent, the reflected and refreacted electromagnetic fields can be neatly treated by the Fresnel equations [3]. For nonideal surfaces, the real physical description is much more complicated. If the surface roughness is small compared with the wavelength of the incident light, it can be treated by the perturbation method for the ideal solution for smooth surfaces. If the scale of the surface toughness is of about the same order as the light wavelength, the

problem is very difficult to deal theoretically. Numerical calculations can only handle it satisfactorily. When the surface irregularity is of a scale much larger than the

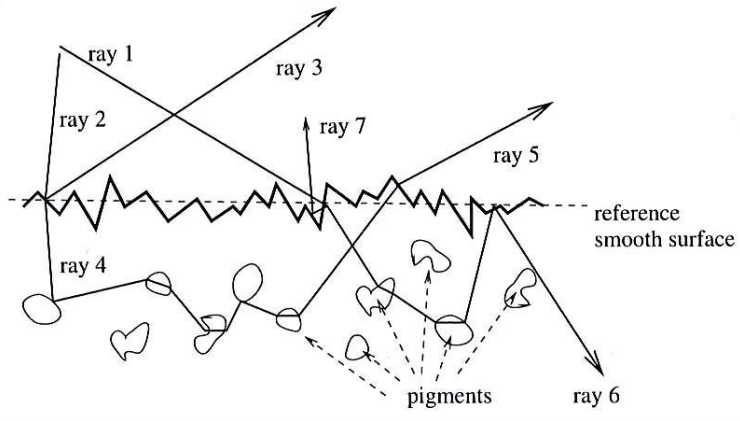

Fig. 2-3 Different components of reflected and refracted light rays.

2.2 Bidirectional Scatter Distribution Function

Basing on radiometry and photometry, the bidirectional transmittance and reflectance distribution functions (BTDF and BRDF) are developed to characterize the optical energy behavior passing through a surface [4-6]. This bidirectional function is a general and useful concept to describe the optical efficiency through geometric relationship between the incoming and outgoing flux.

The geometric relationship of BTDF and BRDF is shown in Fig. 2-4, where the subscripts *i, t,* and *r* denote the incident, reflected and transmitted quality, respectively. Referring to Fig. 2.5, the BTDF and BRDF are defined as the ratio of the outgoing radiance in the viewing direction to the irradiance in the direction of the incident light,

$$BTDF(\theta_i,\phi_i,\theta_t,\phi_t)=\frac{dL_t(\theta_t,\phi_t)}{dE_i(\theta_i,\phi_i)}=\frac{dL_t(\theta_t,\phi_t)}{L_i(\theta_i,\phi_i)\cos\theta_i d\omega_i}, \tag{2.3}$$

and

$$BRDF(\theta_i,\phi_i,\theta_r,\phi_r)=\frac{dL_r(\theta_t,\phi_t)}{dE_i(\theta_i,\phi_i)}=\frac{dL_r(\theta_r,\phi_r)}{L_i(\theta_i,\phi_i)\cos\theta_i d\omega_i}, \tag{2.4}$$

were (θ_i, ϕ_i), (θ_t, ϕ_t), and (θ_r, ϕ_r) are the incident, transmitted and reflected direction

angles with respect to the surface normal.

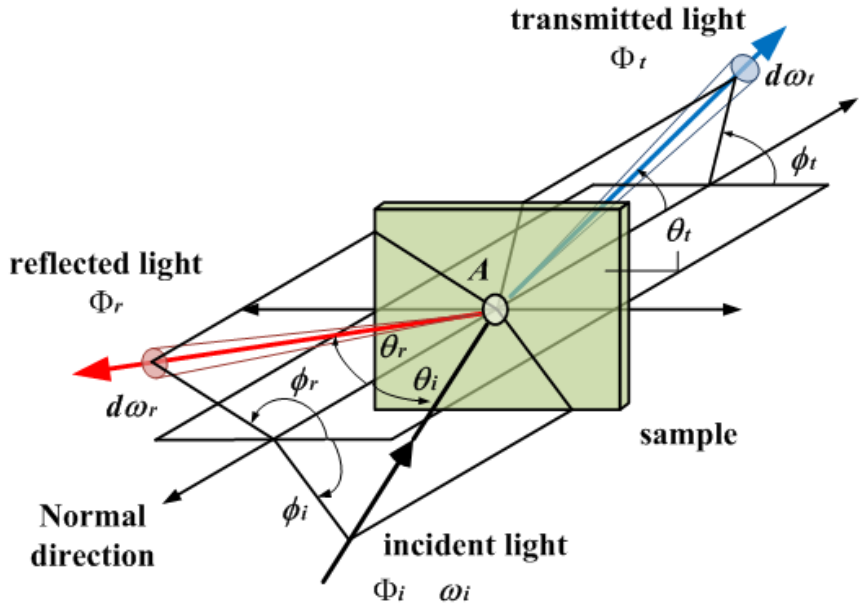

Fig. 2-4 Schematic diagram of BTDF and BRDF.

Although the bidirectional function is quite general and useful, its limitation should be pointed out as well:

1. It is based on the approximation where light propagation is treated as rays.

2. The two quantities, the outgoing radiance *L* and the incident irradiance *E*, should be proportional.

3. The definitions of the BTDF and BRDF assume that the outgoing radiance depends only on the irradiance on the infinitely small area.

In general, fluorescent material cannot be treated by the bidirectional function concept. However, under some conditions, the bidirectional function was presented to be applied on fluorescent material. We proposed this concept to describe the optical characteristics of phosphor in white light emitting diodes (LEDs) in **Chapter 3**.

2.3 Non-paraxial Scalar Diffraction Theory

Before proceeding to measure and analyze the BSDF, we briefly introduce the non-paraxial scalar diffraction theory to illustrate that the diffracted radiance is shift invariant in spherical coordinate. The scattering phenomena are caused by the combination of the diffracted wave, so the scalar diffraction theory can briefly characterize the geometrical properties. It's well known that the irradiance distribution on a plane in the far-field of a diffracting aperture is obtained by the squared modulus of the Fourier transform of the complex amplitude distribution emerging from the aperture :

$$E(\hat{x},\hat{y}) = \frac{1}{\lambda^2 z^2}\left|\Im\left\{U_0^+(x,y)\right\}\Big|_{\xi=\frac{\hat{x}}{\lambda z},\eta=\frac{\hat{y}}{\lambda z}}\right|^2, \tag{2.5}$$

where $U_0^+(x_1,y_1) = U_0^-(x_1,y_1)t_1(x_1,y_1)$ is the complex amplitude distribution emerging from the diffracting aperture with complex amplitude transmittance $t_1(x_1, y_1)$. Implicit in the Fraunhofer approximation is a paraxial limitation which restricts the diffraction angles and incidence angles in a small range. However, the diffracted radiance of non-paraxial diffraction is the fundamental quantity which exhibits shift-invariant behavior.

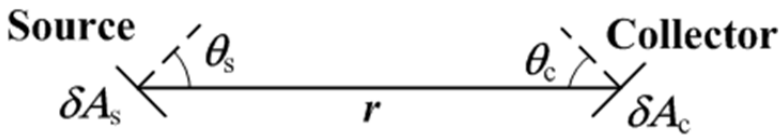

Fig. 2-5 Geometrical configuration used to demonstrate the fundamental theory of radiometry from which the quantity radiance is obtained..

Referring to Eq. 1.2, which defines the radiance, and noting that $\partial\omega_c = \partial A_c \cos\theta_c / r^2$ and $\partial\omega_s = \partial A_s \cos\theta_s / r^2$, we get the double differential

$$\begin{aligned}\partial^2\Phi &= L\partial A_s \cos\theta_s \partial\omega_c \\ &= \frac{L\partial A_s \cos\theta_s \partial A_c \cos\theta_c}{r} \\ &= L\partial\omega_s \partial A_c \cos\theta_c,\end{aligned} \tag{2.6}$$

where r is the distance between the source and the collector, as illustrated in Fig. 2-5. This equation can be considered to be the fundamental theorem of radiometry, as it describes the radiant-power transfer between an elemental source and an elemental collector. If we consider a diffracting aperture as the source and the observation hemisphere as the collector, we can integrate with respect to to the projected source area to obtain the diffracted intensity:

$$I = \frac{\partial\Phi}{\partial\omega_c} = \int_{A_s} L(x,y)\cos\theta_s \partial A_s. \tag{2.7}$$

If we integrate the double differential of Eq. 2.2 with respect to the source's solid angle $\partial\omega_s$, the irradiance on the observation hemisphere (θ_c=0) is just the intensity divided by the square of the radius of the hemisphere:

$$E_c = \frac{\partial\Phi}{\partial A_c} = \int_{\omega_s} L\partial\omega_s = \frac{1}{r^2}\int_{A_s} L\cos\theta_s \partial A_s = \frac{1}{r^2} I. \tag{2.8}$$

From Eq. 1.1, the total radiant power diffracted into the complete hemisphere can be expressed as

$$\begin{aligned}\Phi &= \int_{\Omega_s} I(\theta,\phi) d\omega_c \\ &= \int_\phi \int_\theta I(\theta,\phi)\sin\theta d\theta d\phi \\ &= \int_\alpha \int_\beta I(\alpha,\beta)\frac{d\alpha d\beta}{\gamma}.\end{aligned} \tag{2.9}$$

The direction cosines α, β, and γ are related to the angular variables θ and ϕ in conventional spherical coordinates. The Parseval theorem form Fourier transform theory states that the integral over all space of the squared modulus of any function is equal to the integral over all space of the squared modulus of the Fourier transform of that function. We can write

$$\begin{aligned}\Phi &= \lambda^2 \int_x \int_y \left|U_0(x,y)\right|^2 dxdy \\ &= \lambda^2 \int_\alpha \int_\beta \left|\Im\{U_0(x,y)\}\right|^2 d\alpha d\beta,\end{aligned} \tag{2.10}$$

so the Eq. 2.9 is equal to the right-hand side of this equation:

$$I(\alpha,\beta) = \gamma\lambda^2 \left|\Im\{U_0(x,y)\}\right|^2. \tag{2.11}$$

From Eq. 2.7, we obtain the general equation:

$$\int_{A_s} L(\alpha,\beta,x,y)\cos\theta_s \partial A_s = \gamma\lambda^2 \left|\Im\{U_0(x,y)\}\right|^2. \tag{2.12}$$

If the source is a uniformly illuminated diffracting aperture, there is no dependence on position in the aperture:

$$I(\alpha,\beta) = \int_{A_s} L(\alpha,\beta,x,y)\cos\theta_s \partial A_s \approx L(\alpha,\beta)A_s\cos\theta_s, \tag{2.13}$$

Substituting expression 2.13 into Eq. 2.12, dividing by the area of the diffracting aperture *As*, and recalling that γ cos θ_s, we obtain the following expression for the diffracted radiance:

$$L(\alpha,\beta) = \frac{\lambda^2}{A_s}\left|\Im\{U_0(x,y)\}\right|^2. \tag{2.14}$$

We have thus shown that the squared modulus of the Fourier transform of the complex amplitude distribution emerging from the diffracting aperture yields the diffracted radiance and not the irradiance or the intensity. Furthermore, Eq. 2.14, unlike the more familiar Eq. 2.5, is not restricted to small diffraction angles. From the shift theorem of Fourier transform theory1 it is clear that changes in the angle of incidence of the radiation illuminating the diffracting aperture will merely result in a shift of the radiance function in direction cosine space and an attenuation by the factor γ_0=cos θ_0:

$$L(\alpha,\beta-\beta_0) = \gamma_0 \frac{\lambda^2}{A_s}\left|\Im\{U_0(x,y)\}\, e^{i2\pi\beta_0 y}\right|^2. \tag{2.15}$$

Because the functional form does not change, the diffracted radiance is shift invariant in direction cosine space, and the simple Fourier techniques that have proven to be so

useful in paraxial applications can be used for non-paraxial applications as well.

2.4 BSDF Measurement

To measure the BSDF of a scattering material, there have been two methods to measure the scattering angular field [7]. Analysis of the intensity of scattered light versus direction of light propagation in the hemispherical solid angle above the measurement spot on the sample requires either a mechanical system for motorized scanning of the of viewing directions (or source directions, gonioscopic) or a conoscopic system that projects a collimated beam of light through its front lens on the sample while simultaneously catching all rays reflected from the spot of measurement. In our study, we used the conoscopic approach to implement the BSDF measurement.

2.4.1 Conoscopic approach

A conoscopic system is utilized to measure the angular light distributions of an emitting surface [8]. The optical radiations within wavelength ranges between 380 nm to 780 nm, known as visible light, can be measured. The measuring mode of the conoscopic approach can be classified into transmissive and reflective modes.

Transmissive mode

In transmissive mode (as shown in Fig. 2-6), a Fourier transform lens is adopted to transform the received light into a two-dimensional pattern. Each light ray emitted from the test area in the emitting direction angle, (θ, ϕ) can be focused on the focal plane. Therefore, the directional information of the radiated energy is transferred onto the corresponding position in the focal plane. Then, a relay system is utilized to project this transformed pattern onto a CCD-array detector. In this transformed pattern, each area corresponds to one light radiating direction. Thus, as the pattern is recorded by the CCD-array detector, the optical energy flux and chromaticity in radiating

direction angle (θ, ϕ) are obtained efficiently without mechanical movement.

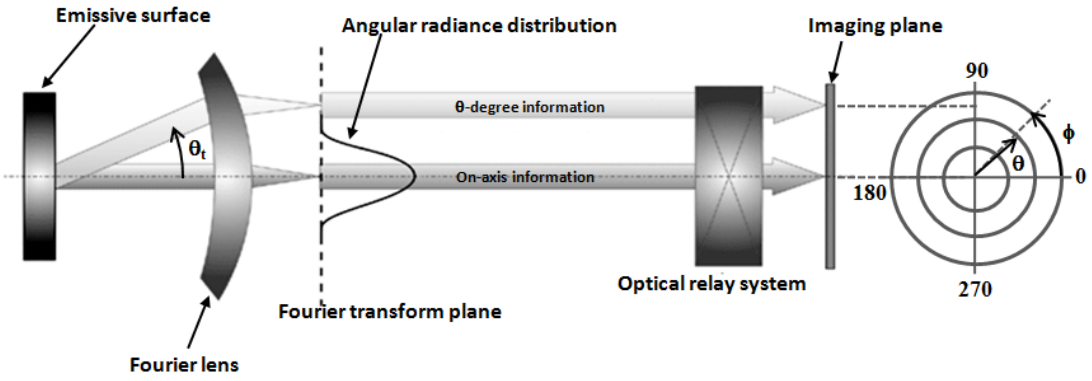

Fig. 2-6 The schematic graph of the conoscopic system in transmissive mode.

Reflective mode

Except the transmissive mode, a reflective mode in the conoscopic system is available to measure the angular distributions of light reflected from samples. In the reflective mode (as shown in Fig. 2-7), a light source emits back from the Fourier transform plane and is inversely focused on the sample under the stage. Here the focused light can be a collimated beam at an incident angle (θ, ϕ) or a diffuse field in all direction by controlling the pupil position and size of the back emitting source on the Fourier transform plane. The light illuminating the sample surface within a tiny illuminated area is reflected back into the Fourier lens. Therefore, the radiance angular distribution of the reflected light is obtained by the CCD-array detector as the transmissive mode.

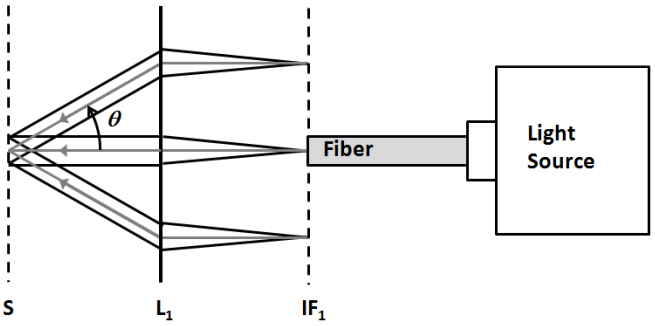

Fig. 2-7 The schematic graph of the conoscopic system in reflective mode.

2.4.2 Experimental setup of BSDF measurement

As Section 2.2 mentioned, BSDF is classified into BRDF and BTDF. From their definitions, a collimated beam induces the sample as an impulse signal, and the measured angular spreading function would relate to the individual incident angle.

For BRDF measurement, the illuminating angle θ of the built-in source is easily varied by controlling the position of the light source with limited pupil size on Fourier transform plane, as Fig. 2-6 shows. In our study, the BRDFs of a scattering surface were obtained by measuring the angular spreading function of different incident angle under the collimated illumination mode of conoscopic system.

To measure the BTDFs, an external light source should be set up to illuminate the back surface of a scattering film. The external light source is schematically shown in Fig. 2-8. Here the collimated beam is produced by a LED combined with a total internal reflection (TIR) lens, and two apertures with 2-mm diameter are used to limit the beam divergent angle within +/- 1 degree. The LED module can slide on an arc track to provide variable incident angle θ. Thus, the geometric relationship of the light source and the angular spreading function is illustrated in Fig. 2-9 (a) and (b), respectively. For a specimen, the collimated beams at different incidence are incident from the illumination hemisphere and the scattering patterns projected on the observing hemisphere are collected by the objective lens of conoscopic system. Fig. 2-10 shows the experimental setup, where the designed light source module is integrated with the conoscopic system in transmissive mode. Through the definition, the BTDF of a scattering film can be recorded and calculated.

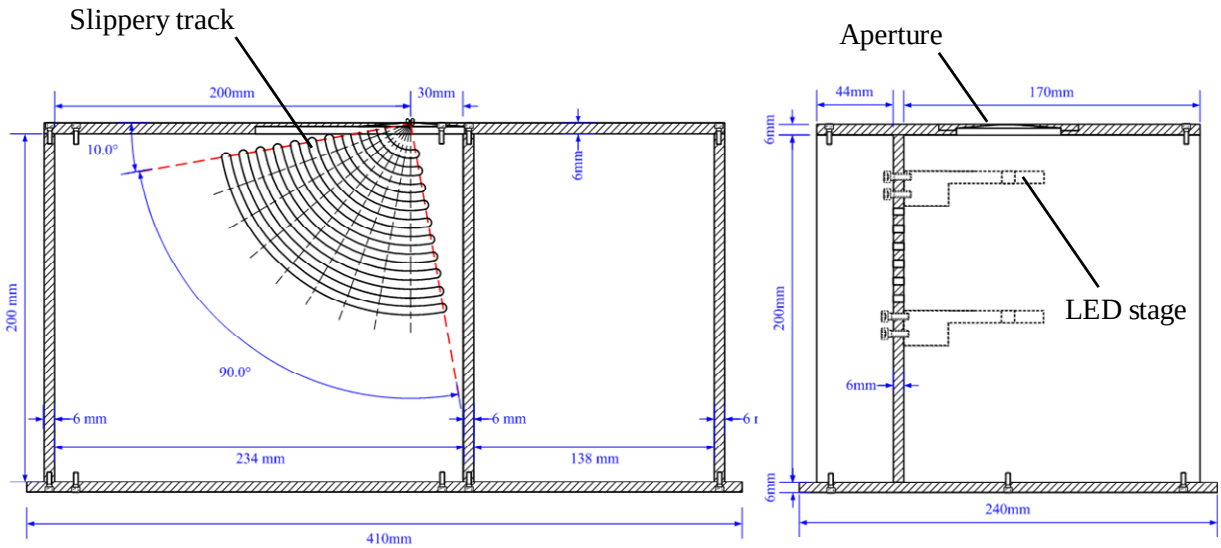

(a) Front view (b) Side view

Fig. 2-8 The scheme of the external light source module for BTDF measurement

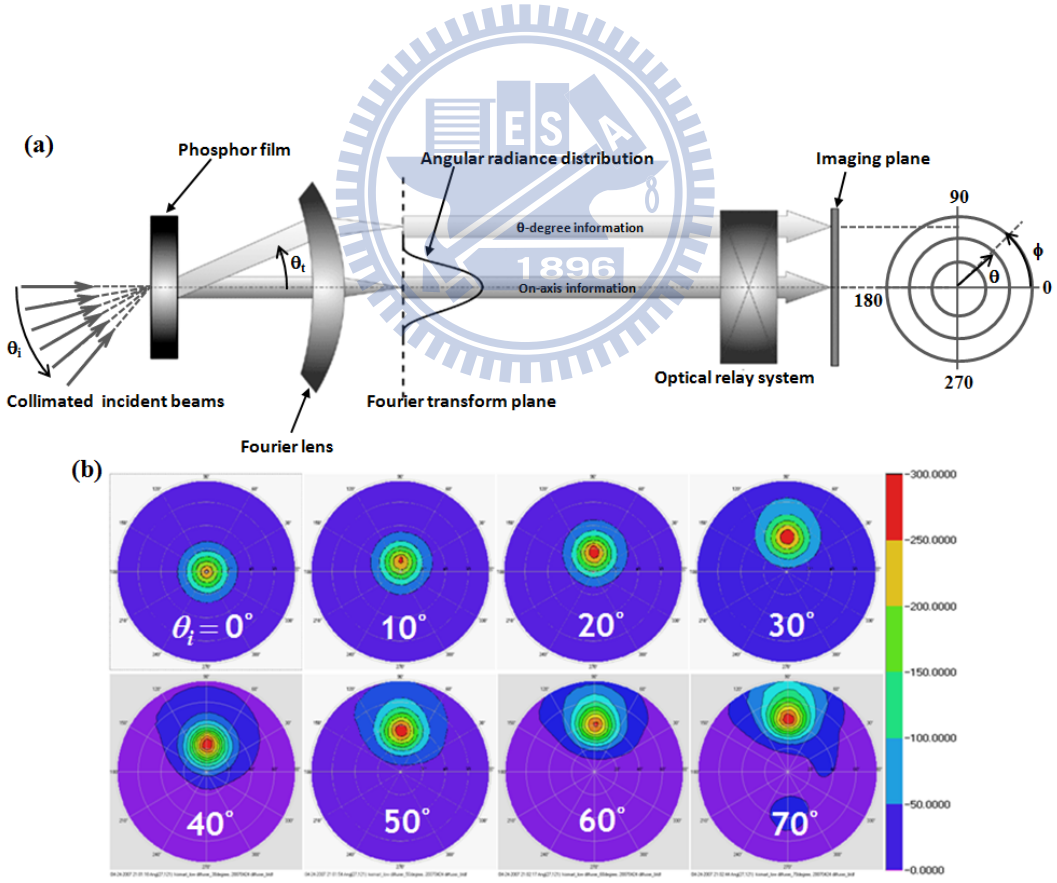

Fig. 2-9 (a) Schematic measurement setup of BTDFs, (b) the measured angular spread functions of an available specimen.

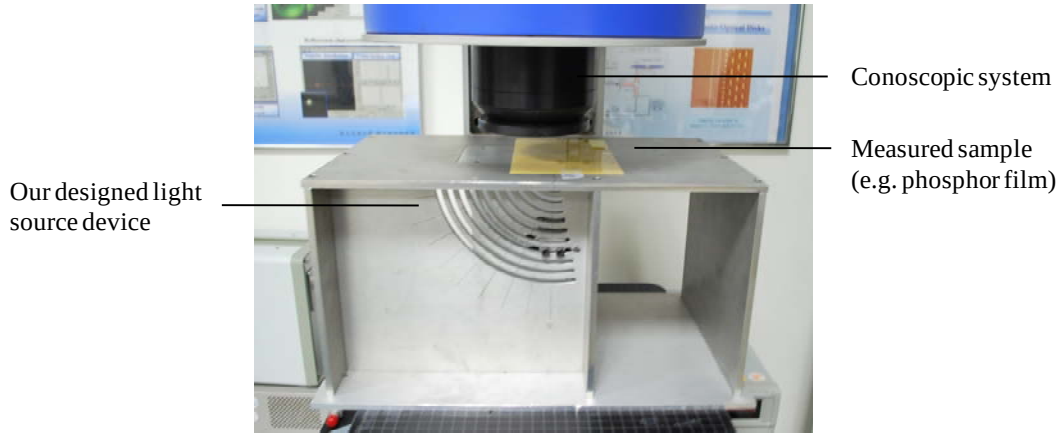

Fig. 2-10 The photograph of BTDF measurement setup.

2.5 BSDF Analysis

BSDFs represent the angular spread function of the scattering specimen, which have a variety of optical features due to various manufacturers' recipes about the refractive index, the density, and the size of scattering particles. In the following, we use the measured BTDFs to analyze two commercial diffusers with different bead sizes. As the tops of Fig. 2-11 (a) and (b) show, the diffusive layer on the top of Polyethylene Terephthalate (PET) substrate has some beads buried in an acrylic binding layer and other diffusing beads protrude partially out of the binder layer. Here the average diameters of the beads are about 10 and 25 μm, respectively. The bottoms of Fig 2-11 illustrate the one-dimensional BTDFs. From the envelope of every transmitted peak, the diffusing power and particle size has a reciprocal relationship. For the case of a laser beam illuminating the diffusing structure with respectively different incident angles, the transmitted angular spectrum can be roughly found by the Fourier transform of the amplitude transmittance function of the bead aperture [9-11]. Thus, the smaller the bead size, the broader the scattering power after passing through the diffuser will be caused. This effect is entirely analogous to the broadening of the angular spectrum with the corresponding special frequency.

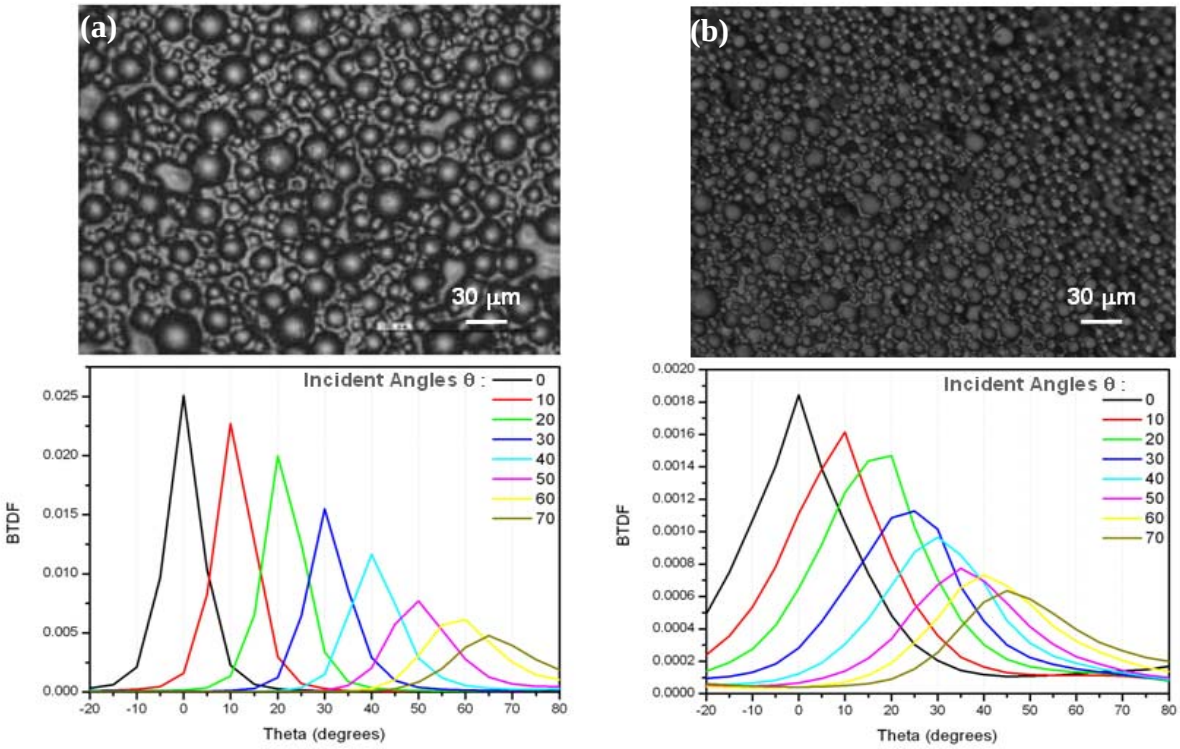

Fig. 2-11. The measured BTDFs and their corresponding OM pictures with (a) low spatial frequency and (b) high spatial frequency.

In addition to the dependence of scattering power on the particle size, there is another issue needed to be mentioned. As the definition, BTDF is simultaneously a function of the incident direction and the transmitted direction. J. E. Harvey [12] has mentioned that a general scattering surface has the shift-invariant behavior, which just requires one set of numerical data to completely characterize the scattering properties of a surface. The most conventional diffusers are circularly symmetric, so the variations of the incident impulse along azimuthal angle ϕ would be ignored. However, as shown in Fig 2-11, the BTDFs exhibit a discrepant scattering shape and peak shift with different inclining illumination. Especially, the phenomena are more observable in larger angles of incidence. Thus, in the incident side, BTDF is a function of pure inclination θ.

2.6 References

[1] New Buildings Institute, Inc. Advanced Lighting Guidelines (2003)

[2] John. C. Stover, *Optical Scattering: Measurement and Analysis*, (Mc Graw-Hill, New York, 1990).

[3] E. Hecht, Optics, 2nd edition, (Addison-Wesley, MA, 1987).

[4] F. E. Nicodemus, J. C. Richmond, J. J. Hsia, I. W. Ginsberg, and T. Limperis, *Geometric Considerations and Nomenclature for Reflectance*, (U.S. Dept. Commerce, Washington, D.C., NBS Monograph 160, 1977).

[5] Commission Internationale de l'Eclairage, Radiometric and Photometric Characteristics of Materials and their Measurement, 2ndEdition, (CIE 38 (TC-2.3), Paris, 1977).

[6] M. Bass, E. W. Van Stryland, D. R. Williams and W. L. Wolfe, *Handbook of Optics*, *Volume II*, (McGraw-Hill, New York, 1991).

[7] M. E. Becker, "Display Reflectance: Basics, Measurement, and Rating," J. SID **14/11**, 1003-1017 (2006).

[8] M. E. Becker, "Evaluation and characterization of display reflectance," Displays **19**, 35-54 (1998).

[9] Joseph W. Goodman, *Introduction to Fourier Optics*, (McGraw-Hill, New York, 2004)

[10] Keigo Iizuka, *Elements of Photonics I,* (Willey, New York, 2002)

[11] A. M. Nuijs and J. J. L. Horikx, "Diffraction and scattering at antiglare structures for display devices," Appl. Opt. **33**, 4058-4068 (1994).

[12] J. E. Harvey and Cynthia L. Vernold, "Transfer Function Characterization of Scattering Surface," Proc. SPIE **3141**, 113–127 (1997).

Chapter 3

Dichromatic BSDF

BSDFs usually describe the optical mechanisms of the reflection, transmission, and scatter. We attempt to characterize the fluorescence properties of the emissive material by BSDF. Thus, the polychromatic BSDF is proposed, and a commercial pcLED was measured to verify the proposed model by dichromatic consideration. The concepts, definitions, and measurement methods of the polychromatic BSDFs were presented and demonstrated in this chapter.

3.1 Phosphor-converted LED

The wavelength converting schemes have been widely used in many illuminating subjects, including cold cathode fluorescent lamps (CCFLs), plasma emission devices, and phosphor-converted light-emitting diodes (pcLEDs). Over the variety of applications, the rapid progress of pcLEDs has attracted much attention due to the emerging LED lighting market. The most general pcLED schemes use the broadband yellow phosphor (yttrium aluminum garnet: YAG) to absorb the blue-light flux from a GaN chip and generate the white light by mixing the die-emitted blue light with the phosphor-converted yellow light [1]. In additional to the phosphor improvement, the configuration of pcLEDs was also evolved from the conventional scheme, where the YAG powder phosphor is directly coated on the GaN surface [2,3], to the remote phosphor approaches. The separation of the phosphor from the LED surface was firstly proposed as the scattered photon extraction (SPE) structure by *N. Narendran* et

al. to enhance the extraction efficiency [4]. After that, the multi-functional consideration including the remote phosphor, diffuse reflector cup, and hemispherical dome was further designed to minimize the guided radiant flux inside the LED [5]. The concepts of the remote phosphor separated by an air gap from the blue LED were addressed to achieve various targets, such as highly uniform planar source [6,7], and enhanced light extraction by internal reflection [8,9].

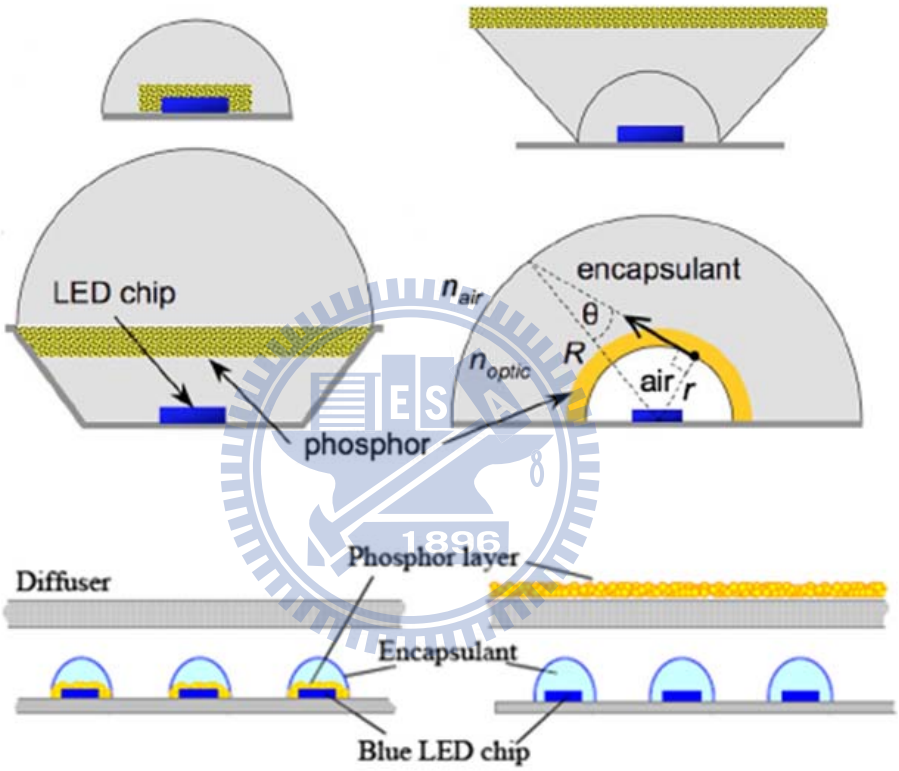

Fig. 3-1 Schematic configurations of pcLEDs.

The phosphor material absorbs energy in a region of wavelengths and then re-emits the energy in a region of longer wavelengths. In terms of the pcLEDs, because the phosphor-scattered blue light and phosphor-emitted yellow light have different radiant intensity distributions, there is a non-uniform angular color distribution. Few studies have attempted to characterize the optical properties of the

YAG phosphor in the pcLEDs due to the massive quantities of measurement and underlying complicated physical processes. K. Yamada et al. simulated the YAG phosphor film in a pcLED by defining the transmitted and reflected flux of the blue and yellow light, respectively [10]. Although they analyzed the pcLED structure by the optical simulation with the measured phosphor properties, the accuracy of the simulated results was not verified. Zhu et al. also used two integrating spheres to measure the amount of transmitted and reflected power for characterizing the optical throughput of a YAG phosphor slide, which was illuminated by a fiber-guided source [11]. However, the interaction of the illuminating energy with the phosphor would not just behave as a simple wavelength-converting phenomenon, but also a function of the illuminating and viewing geometry. In other words, the description of the phosphor-light interaction shall be associated with wavelength as well as geometric considerations, which can't be merely defines by the transmitted or reflected flux. Furthermore, the fiber-produced light sources in the references are not appropriate to be involved as the LED chip-emitted field. A general and complete description of such wavelength-converting properties should be defined for the incident light fields of the various LED configurations.

In this study, we propose a simple but effective description to characterize the optical properties of the phosphor layer in the pcLEDs by using the measured bidirectional scattering distribution functions (BSDFs), which are regarded as the angular impulse responses of a phosphor layer. The BSDF characterization can completely describe the energy behavior by direction and wavelength. The characterizing methodology and its measurement are introduced. Finally, a commercially available pcLED with the conformal phosphor coating was examined to validate the proposed methodology accordingly.

3.2 Dichromatic BSDF

3.2.1 Energy Balance Equation

To characterize the phosphor in a pcLED sample, the BSDFs was adopted to define the general description of light propagation with the angular and wavelength variables [12, 13]. However, the optical properties are prohibitively complicated and lead to massive quantities of data. In order to avoid the explosion of photometric data, some conditions were assumed:

1. The geometrical configuration of phosphor is treated as a thin-layer approximation, including a forward and backward surface related to the LED chip.
2. The optical features of the phosphor include the wavelength conversion and scatter.
3. The relation of the incident and outgoing flux satisfies scalability and addictivity due to the linear conversion between the LED-emitted and phosphor-emitted spectral power distribution.

In this chapter, the forward mode was expressed in the equations. The associated photometric and geometric quantities in polar coordinates are illustrated in Fig. 3-2, where all the scientific symbols and terminology through this paper are listed in Table 3-1.

First of all, the energy balance equation in **Chapter 1** for a radiating surface is recalled by the following equation:

$$\underbrace{L(x,y,\theta_t,\phi_t)}_{\text{total radiance}} = \underbrace{L_s(x,y,\theta_t,\phi_t)}_{\text{physical scenes}} + \underbrace{L_e(x,y,\theta_t,\phi_t)}_{\text{emitted radiance}}, \tag{3.1}$$

where L, L_e ,and L_s are the total radiance, the emitted radiance, and the non-emitted (scattered) radiance leaving point (x, y) in transmitting-side direction (θ_t, ϕ_t). Here we assume that the phosphor layer is homogenous, the position (x, y) is not included as

parameter. Based on the wavelength conversion mechanisms of pcLEDs, the energy balance equation of the phosphor is composed of three terms:

$$\begin{aligned} L(\theta_t,\phi_t) &= L_{fs}^{B}(\theta_t,\phi_t) + L_{fe}^{Y}(\theta_t,\phi_t) + L_{fs}^{Y}(\theta_t,\phi_t) \\ &= \int_{\Omega_i} \left[(\rho_{fs}^{B-B} + \rho_{fe}^{B-Y}) L_i^{B}(\theta_i,\phi_i) + \rho_{fs}^{Y-Y} L_i^{Y}(\theta_i,\phi_i) \right] \cos\theta_i d\omega_i, \end{aligned} \tag{3.2}$$

where L_{fs}^{B}, L_{fe}^{Y}, and L_{fs}^{Y} indicate the forward-scattered blue-light, forward-emitted yellow-light, and forward-scattered yellow-light radiance, respectively. As the equation shows, the three transmitting radiance terms are obtained by the integration of the incident blue-light radiance L_i^{B} and yellow-light radiance L_i^{Y} over the full solid angle Ω_i of the incident hemisphere. Here the weights, $\rho_{fs}^{B\text{-}B}$, $\rho_{fe}^{B\text{-}Y}$, and $\rho_{fs}^{Y\text{-}Y}$, represent the bidirectional photometric data with blue-to-blue, blue-to-yellow, and yellow-to-yellow pairs, respectively.

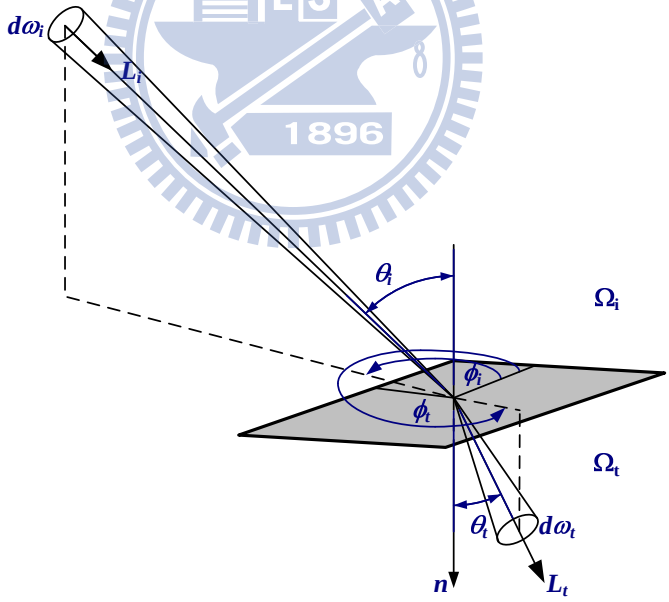

Fig. 3-2. Photometric and geometric quantities in the polar

Table 3-1. Nomenclature

Abbreviations		*Subscripts*	
L	radiance (W/sr*m^2)	***i***	Incident
I	radiant intensity (W/sr)	***t***	Transmitted
Φ	light flux (W)	***B***	blue light
P	spectral radiance (W/sr*m^3)	***Y***	yellow light
ρ	bidirectional function (sr^{-1})	***fs***	forward scattered
ω, Ω	solid angle (sr)	***fe***	forward emitted
θ, ϕ	polar coordinates	***bs***	backward scattered
λ	wavelength	***be***	backward emitted

3.2.2 Blue-to-blue radiance L_{fs}^{B}

In terms of the non-emitted radiance, the forward scattered blue-light radiance, L_{fs}^{B}, is determined by the incident radiance L_i^B and blue-to-blue bidirectional distribution function $\rho_{fs}^{B\text{-}B}$,

$$L_{fs}^{B}(\theta_t,\phi_t)=\int_{\Omega_i}\rho_{fs}^{B-B}(\theta_i,\phi_i,\theta_t,\phi_t)L_i^B(\theta_i,\phi_i)\cos\theta_i d\omega_i. \tag{3.3}$$

where $\rho_{fs}^{B\text{-}B}$ is defined by the ratio of the transmitted radiance dL_{fs}^{B} in the transmitted direction (θ_t, ϕ_t) to the irradiance dE_i^B in an incident direction (θ_i, ϕ_i),

$$\rho_{fs}^{B-B}(\theta_i,\phi_i,\theta_t,\phi_t)=\frac{dL_{fs}^{B}(\theta_t,\phi_t)}{dE_i^B(\theta_i,\phi_i)}=\frac{dL_{fs}^{B}(\theta_t,\phi_t)}{L_i^B(\theta_i,\phi_i)\cos\theta_i d\omega_i}, \tag{3.4}$$

For pcLEDs, the GaN LED serves as the excitation source with a specific spectral power distribution $P_i^B(\lambda)$. In terms of blue-to-blue radiance, the role of phosphor is a typical scattering material. Thus, the phosphor-scattered radiance has a spectral power distribution $P_{fs}^{B}(\lambda)$ which is identical to that of the incident light peaking around 450 nm. Fig. 3-3 shows the normally incident spectrum $P_i^B(\lambda)$ of illumination and the transmitted spectrum $P_{fs}^{B}(\lambda)$ detected in the normal direction of the phosphor layer by

the experimental measurement.

Thus, the L_i^B and L_{fs}^B in Eq. 4 were derived by the integration of the measured $P_i^B(\lambda)$ and $P_{fs}^B(\lambda)$ over the blue-light wavelength region (400-500 nm),

$$\rho_{fs}^{B-B}(\theta_i,\phi_i,\theta_t,\phi_t)\begin{cases} L_i^B(\theta_i,\phi_i) = \int\limits_{\text{Blue-light Region}} P_i^B(\theta_i,\phi_i,\lambda)d\lambda \\ L_{fs}^B(\theta_t,\phi_t) = \int\limits_{\text{Blue-light Region}} P_{fs}^B(\theta_t,\phi_t,\lambda)d\lambda \end{cases}. \tag{3.5}$$

Here the spectral BSDFs, ρ_{fs}^{B-B}, can be regarded as the angular spreading function with spectrum dependence.

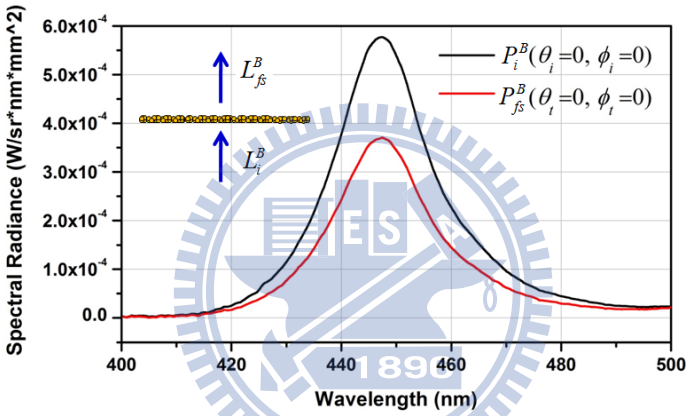

Fig. 3-3. The normal illumination $P_i^B(\lambda)$ and the normal viewing $P_{fs}^B(\lambda)$

3.2.3 Blue-to-yellow radiance L_{fe}^Y

The second term on the Eq. 3.2, L_{fe}^Y, represents the emitted radiance subject to wavelength conversion by the phosphor layer. In general, the converting efficiency of the phosphor is merely determined by the energy-based quantity. As the spatial dependence is considered, a more complete discussion including directional function is included. For pcLEDs, the phosphor-converted efficiency obeys scalability and addictivity due to the unique relation of chip-emitted and phosphor-emitted spectral distribution. The forward emitted radiance L_{fe}^Y can be linearly related to the incident radiance L_i^B and blue-to-yellow bidirectional distribution function ρ_{fe}^{B-Y},

$$L_{fe}^{Y}(\theta_t,\phi_t)=\int_{\Omega_i}\rho_{fe}^{B-Y}(\theta_i,\phi_i,\theta_t,\phi_t)L_i^{B}(\theta_i,\phi_i)\cos\theta_i d\omega_i. \tag{3.6}$$

where the $\rho_{fe}^{B\text{-}Y}$ is defined as the ratio of the transmitted radiance dL_{fe}^{Y} in the transmitted direction to the irradiance dE_i^{B} in an incident direction,

$$\rho_{fe}^{B-Y}(\theta_i,\phi_i,\theta_t,\phi_t)=\frac{dL_{fe}^{Y}(\theta_t,\phi_t)}{dE_i^{B}(\theta_i,\phi_i)}=\frac{dL_{fe}^{Y}(\theta_t,\phi_t)}{L_i^{B}(\theta_i,\phi_i)\cos\theta_i d\omega_i}, \tag{3.7}$$

Different from the blue-to-blue radiance, behavior of the forward emitted spectral distribution $P_{fe}^{Y}(\lambda)$ depends on the phosphor conversion properties. Thus, the $\rho_{fe}^{B\text{-}Y}$ shall be obtained by the wavelength integration over different spectral regions separated by blue (400-500 nm) and yellow (500-750nm), respectively.

$$\rho_{fe}^{B-Y}(\theta_i,\phi_i,\theta_t,\phi_t)\begin{cases}L_i^{B}(\theta,\phi)=\int_{\text{Blue-light Region}}P_i^{B}(\theta,\phi,\lambda)d\lambda\\ L_{fe}^{Y}(\theta,\phi)=\int_{\text{Yellow-light Region}}P_{fe}^{Y}(\theta,\phi,\lambda)d\lambda\end{cases}. \tag{3.8}$$

As a set of the measured spectral radiance distribution in Fig. 3-4, the emitted spectrum $P_{fe}^{Y}(\lambda)$ has a broad spectral distribution over the region of yellow-light. Therefore, the down converting phenomena of the phosphor conversion can be simultaneously described by the dichromatic BSDFs.

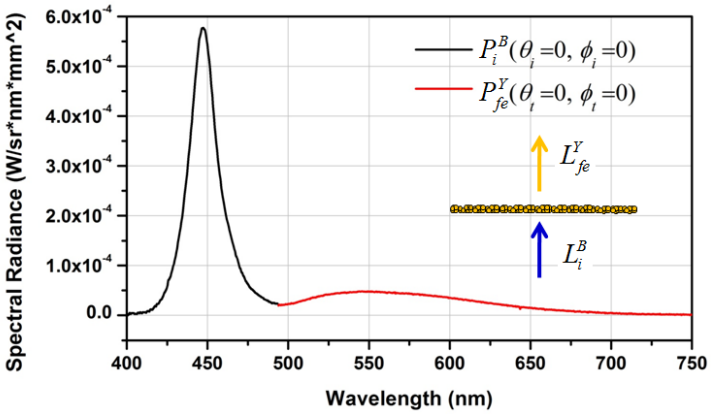

Fig. 3-4. The normal illumination $P_i^{B}(\lambda)$ and the normal viewing $P_{fe}^{Y}(\lambda)$

3.2.4 Yellow-to-yellow radiance L_{fs}^{Y}

In addition to the incident radiance L_i^B from GaN LED, the backward phosphor-emitted yellow light can be recycled to induce additional forward scattering in the phosphor layer. To characterize this effect, the non-emitted (scattered) radiance of the energy balance equation Eq. 3.1 shall take account of recycled radiation, as the third term in Eq. 3.2. Similar to aforementioned manipulation, the recycling radiance L_{fs}^{Y} can be described by the integration of incident light L_i^Y with the yellow-to yellow bidirectional distribution function $\rho_{fs}^{Y\text{-}Y}$

$$L_{fs}^{Y}(\theta_t,\phi_t)=\int_{\Omega_i}\rho_{fs}^{Y-Y}(\theta_i,\phi_i,\theta_t,\phi_t)L_i^{Y}(\theta_i,\phi_i)\cos\theta_i d\omega_i, \tag{3.9}$$

where $\rho_{fs}^{Y\text{-}Y}$ is defined as

$$\rho_{fs}^{Y-Y}(\theta_i,\phi_i,\theta_t,\phi_t)=\frac{dL_{fs}^{Y}(\theta_t,\phi_t)}{dE_i^{Y}(\theta_i,\phi_i)}=\frac{dL_{fs}^{Y}(\theta_t,\phi_t)}{L_i^{Y}(\theta_i,\phi_i)\cos\theta_i d\omega_i}. \tag{3.10}$$

As the blue-to-blue bidirectional distribution function $\rho_{fs}^{B\text{-}B}$ introduced in Section 2.2, the $\rho_{fs}^{Y\text{-}Y}$ is obtained by the integrations of the spectral distributions $P_i^{Y}(\lambda)$ and $P_{fs}^{Y}(\lambda)$ over the yellow-light region (500-750 nm),

$$\rho_{fs}^{Y-Y}(\theta_i,\phi_i,\theta_t,\phi_t)\begin{cases}L_i^{Y}(\theta,\phi)=\int\limits_{\substack{\text{Yellow-light}\\ \text{Region}}}P_i^{Y}(\theta,\phi,\lambda)d\lambda\\ L_{fs}^{Y}(\theta,\phi)=\int\limits_{\substack{\text{Yellow-light}\\ \text{Region}}}P_{fs}^{Y}(\theta,\phi,\lambda)d\lambda\end{cases}. \tag{3.11}$$

A sample of the measured spectral distributions $P_i^{Y}(\lambda)$ and $P_{fs}^{Y}(\lambda)$ were conducted, as shown in Fig. 3-5. It is important to note that the spectral BSDFs are highly relevant to the phosphor recipes, wavelength and illumination/viewing geometry. Different specimens and illuminating sources would exhibit discrepant BSDFs.

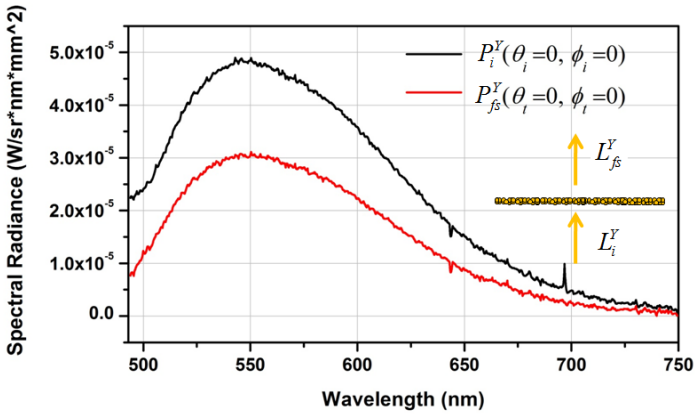

Fig. 3-5. The normally-illuminating $P_i^Y(\lambda)$ and the normally-detected $P_{fs}^Y(\lambda)$

3.2.5 Radiance Integration

To summarize the aforementioned manipulation about phosphor characterization, the dichromatic BSDF was contributed by the three independent components: $\rho_{fs}^{B\text{-}B}$, $\rho_{fe}^{B\text{-}Y}$, and $\rho_{fs}^{Y\text{-}Y}$.

$$\rho_D(\theta_i,\phi_i,\theta_t,\phi_t)=\rho_{fs}^{B-B}(\theta_i,\phi_i,\theta_t,\phi_t)+\rho_{fe}^{B-Y}(\theta_i,\phi_i,\theta_t,\phi_t)+\rho_{fs}^{Y-Y}(\theta_i,\phi_i,\theta_t,\phi_t), \quad (3.12)$$

In additional to the dichromatic white mixing scheme, the description can be extended to a general form with the polychromatic radiance,

$$\begin{aligned}\rho_P(\theta_i,\phi_i,\theta_t,\phi_t)&=\rho_{fs}^{\lambda_0-\lambda_0}(\theta_i,\phi_i,\theta_t,\phi_t)\\&+\sum_m(\rho_{fe}^{\lambda_0-\lambda_m}(\theta_i,\phi_i,\theta_t,\phi_t)+\rho_{fs}^{\lambda_m-\lambda_m}(\theta_i,\phi_i,\theta_t,\phi_t)).\end{aligned} \quad (3.13)$$

where λ_0 is the wavelength of the light source, such as the blue light from the GaN LEDs. The index m represents m-th emitted spectrum which depends on the light source and the converting properties of the phosphor. Therefore, the energy balance equation is modified by the polychromatic BSDF as an integral equation:

$$L(\theta_t,\phi_t)=\int_{\Omega_i}\rho_P(\theta_i,\phi_i,\theta_t,\phi_t)L_i(\theta_i,\phi_i)\cos\theta_i d\omega_i. \quad (3.14)$$

Through the characterizations of the dichromatic BSDFs, the transmitting-side optical properties of a phosphor layer in a pcLED can be numerically obtained by the integration (Eq. 3.2) Several studies have been proposed to tackle the radiance integration [12, 13]. Among the various approaches, the Monte Carlo method is most common and available from the commercial simulation tools [14]. Here we used a Monte Carlo method based computational tool, LightTools™, to implement the integration.

3.3 Experiment

3.3.1 BSDFs measurement

The spectral BSDFs of a YAG phosphor layer were measured by the conoscopic approach associated with an in-house light source module as aforementioned in **Chapter 2**. Because of the rotationally symmetric properties of the YAG phosphor layer, the two-dimensional illumination sampling for the BSDFs measurement can be reduced to one-dimensional illumination scanning. As the schematic illustration in Fig. 3-6 (a), the specimen was illuminated by a collimated beam with a set of discrete incident directions $\theta_{i,}$, and the corresponding angular spread function can be collected by the objective lens with the moderate numerical aperture for the observation of the imaged plane. Fig. 3-6 (b) shows one set of the measured angular spread functions of a test specimen with the different incident angles θ_i along a constant azimuthal direction $\phi_i = 90^o$. Every incident beam illuminating the specimen would lead to an angular spread function. As the measured BSDFs vary smoothly under different incident angles $\theta_{i,}$, the angular sampling is adequate to completely characterize the scattering behavior. The BSDFs are highly relevant to the geometric natures of the phosphor particulates.

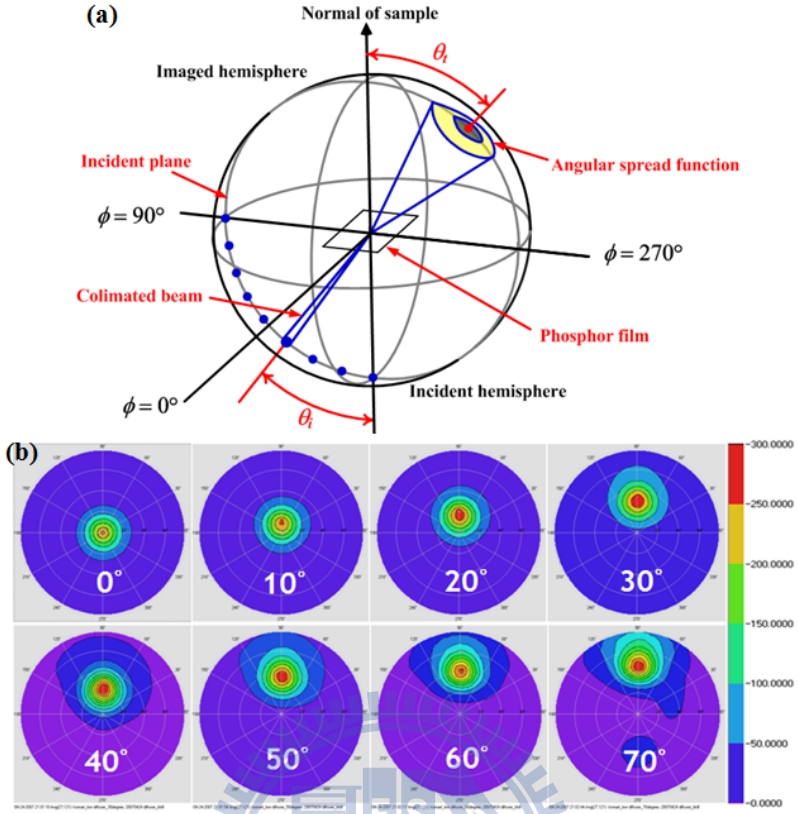

Fig. 3-6. (a) Schematic measurement setup of BSDFs, (b) the measured angular spread functions of an available specimen.

In order to obtain the spectral BSDFs ρ in Eq. 3.12, three components were individually measured. First of all, the collimated incident beams with the designated spectral radiance distributions $P_i^B(\lambda)$ or $P_i^Y(\lambda)$ was set to illuminate the YAG phosphor film, where phosphor was coated on a thin substrate with identical coating parameters. Then, the spectrophotometric measurement was executed by scanning over the imaging plane of the conoscopic system to obtain the corresponding spectral radiance distribution, $P_{fs}^B(\theta_t,\phi_t,\lambda)$, $P_{fe}^Y(\theta_t,\phi_t,\lambda)$, $P_{fs}^Y(\theta_t,\phi_t,\lambda)$, accordingly. Fig. 3-7 shows the measured results of $P_{fs}^B(\theta_t,\lambda)$ and $P_{fe}^Y(\theta_t,\lambda)$, where the spectrometer scanned over the θ_t direction with 5-degree intervals under the normal illumination condition of the blue LED source. Based on the definition of dichromatic BSDF, the

scattered and the emitted angular spread function can be separated by the integration boundary of the measured spectral distributions. Fig. 3-8 (a)-(c) show the measured $\rho_{fs}^{B\text{-}B}$, $\rho_{fe}^{B\text{-}Y}$, and $\rho_{fs}^{Y\text{-}Y}$ of the considered phosphor film. In addition to the forward radiance in the transmitting hemisphere of the phosphor layer, the backward components, $\rho_{bs}^{B\text{-}B}$, $\rho_{be}^{B\text{-}Y}$, and $\rho_{bs}^{Y\text{-}Y}$, can be obtained via the same procedure as well.

The dichromatic BSDFs also provide a figure of merit to qualitatively examine the optical properties of the phosphor film. The spectral BSDFs are highly dependent on the recipe and micro-feature of the phosphor layer, different manufactures will have their own BSDFs. In this case, the transmitted angular distribution in Fig. 3-8 (a) and (c) is concentrated in a relatively narrow angular range with shift variant properties. On the other hand, blue-to-yellow bidirectional distribution functions in Fig. 7 (b) implies the wavelength conversion mechanism effectively leave the YAG phosphor layer as a near Lambertian field.

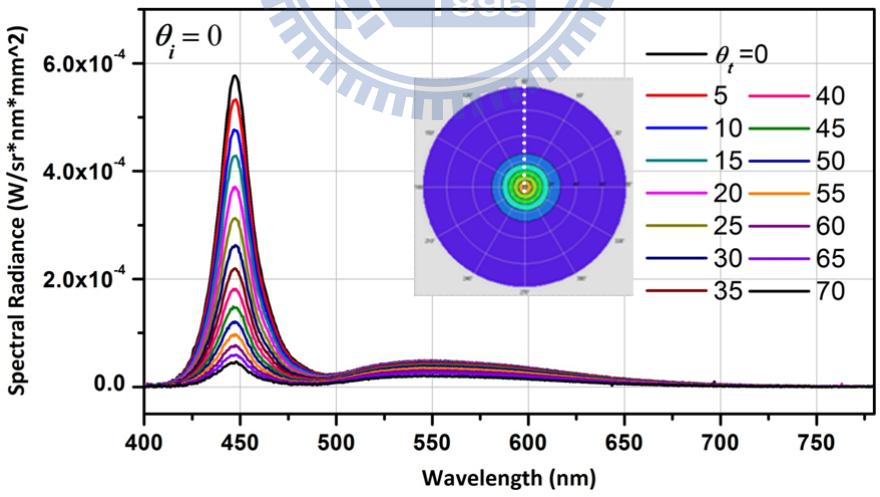

Fig. 3-7. The measured results of $P_{fs}^{B}(\theta_t, \lambda)$ and $P_{fe}^{Y}(\theta_t, \lambda)$ under normal illumination

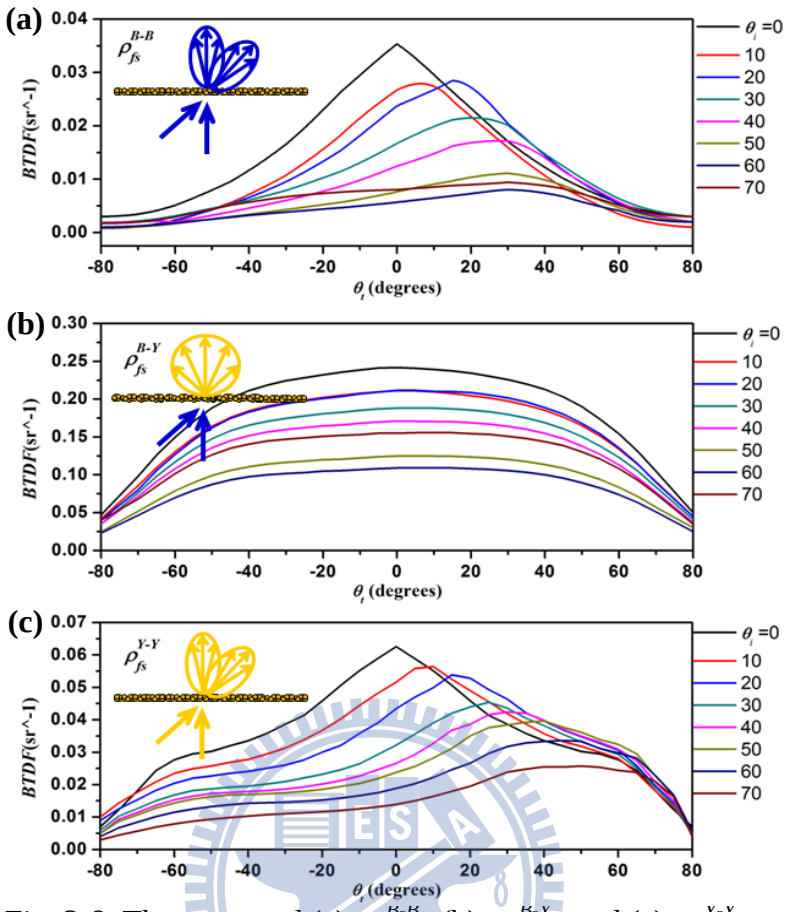

Fig. 3-8. The measured (a) $\rho_{fs}^{B\text{-}B}$, (b) $\rho_{fe}^{B\text{-}Y}$, and (c) $\rho_{fs}^{Y\text{-}Y}$.

3.3.2 Verification

In order to validate the phosphor characterization, a commercially available pcLED with conformal phosphor coating was examined. Firstly, the BSDF measurement of the YAG phosphor coated on PET substrate was conducted, where the coating method and recipe of the phosphor were identical to that in chip-level. Then we imported the measured bidirectional photometric data (in Section 3.1) into the simulation with GaN blue LED chip (0.5×0.5 mm^2) to predict both blue and yellow radiant intensity distribution. The inset of Fig. 8 shows the measured pcLED, where the phosphor coated on the blue LED chip (0.5×0.5 mm) was fabricated by the pulsed spray coating method [15]. Because of the consideration of the multi-wavelength emission, the simulation was performed in multi-steps. After

summing the simulated results of each wavelength, the simulated far-field luminous intensity distribution and angular correlated color temperature (CCT) distribution (see in Appendix) are shown in Fig. 3-9 (a) and (b), respectively [16]. Comparing with the experimental measurements, the numerical predictions have 98.9% and 97.9% correlation with the practical results. The CCT deviations are mainly resulted from the BSDF measurement errors attributed by the distortion of conoscopic system. After the energy superposition of Eq. 2, the BSDF errors would be cumulated. Despite the deviations, the simulated CCT distribution curve still provides useful information to evaluate the color uniformity of a pcLED configuration. The close agreement of the measurement demonstrated the validity of the proposed model for phosphor description in the pcLED applications.

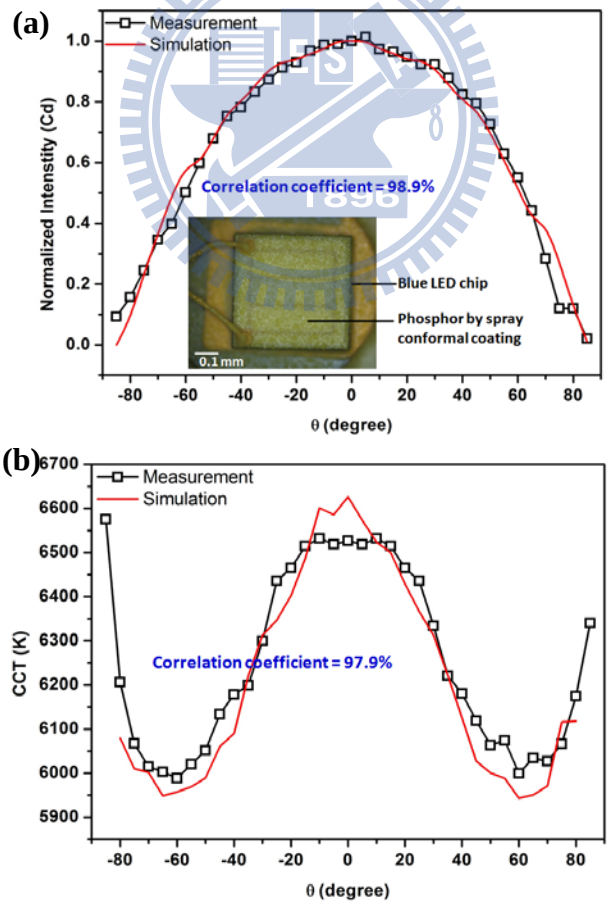

Fig. 3-9 The simulated (a) luminous intensity distribution and (b) angular CCT distribution

3.4 Summary

A simple but effective phosphor modeling of the pcLED is proposed. The major advantage of this study lies in that there is no need to formulate the complex physical mechanism of the phosphor scattering in a microscopic viewpoint. Instead, as long as the coated phosphor layer is available, the proposed methodology assisted by the measured BSDFs is able to characterize the phosphor properties with the direction and wavelength variables. By the Monte Carlo simulation, pcLED luminous intensity distribution and its angular CCT distribution can be predicted with high accuracy. Closed agreement with a commercially available pcLED validates the proposed scheme, which certainly has impact for the LED development in illumination applications.

3.5 References

[1] S. Nakamura and G. Fasol. *The Blue Laser Diode: GaN Based Light Emitters and Lasers*, (Springer-Verlag, New York, 1997).

[2] R. Mueller-Mach, G. O. Mueller, M. R. Krames, and T. Trottier, "High-power phosphor-converted light-emitting diodes based on III-nitrides" IEEE J. Sel. Top. Quantum Electron. **8**, 339-345 (2002).

[3] http://www.philipslumileds.com/technology/whitelighting.cfm

[4] N. Narendran, Y. Gu, J. P. Freyssinier-Nova, and Y. Zhu, "Extracting phosphor-scattered photons to improve white LEDs efficiency," Phys. Status Solid A **202**, R60-R62 (2005).

[5] H. Luo, J. K. Kim, E. F. Schubert, J. Cho, C. Sone, and Y. Park, "Analysis of high-power packages for phosphor based white-light-emitting diodes," Appl. Phys. Lett. **86**, 243505 (2005).

[6] Y. Ito, T. Tsukahara, S. Masuda, T. Yoshida, N. Nada, T. Igarashi, T. Kusunoki, and J. Ohsako, "Optical design of phosphor sheet structure in LED backlight system," SID Int. Symp. Digest Tech. Papers **39**, 866-869, (2008).

[7] C.-H. Tien, C.-H. Hung , B.-W. Xiao, H.-T. Huang, Y.-P. Huang, and C.-C. Tsai, "Planar lighting by blue LEDs array with remote phosphor," Proc. SPIE **7617**, 761707 (2010)

[8] S. C. Allen and A. J. Steckl, "ELiXIR—Solid-state luminaire with enhanced light extraction by internal reflection," J. Disp. Technol. **3**, 155-159 (2007).

[9] S. C. Allen and A. J. Steckl, "A nearly ideal phosphor-converted white light-emitting diode," Appl. Phys. Lett. **92**, 143309 (2008).

[10] K. Yamada, Y. Imai, and K. Ishi, "Optical simulation of light source devices composed of blue LEDs and YAG phosphor," J. Light & Vis. Env. **27**, 70-74 (2003).

[11] Y. Zhu, N. Narendran, and Y. Gu. "Investigation of the optical properties of YAG: Ce phosphor," Proc. SPIE **6337** (2006).

[12] J. de Boer, "Modelling indoor illumination by complex fenestration systems based on bidirectional photometric data," Energy and Buildings **38,** 849–868 (2006).

[13] C.-H. Tien, and C.-H. Hung, "An iterative model of diffuse illumination from bidirectional photometric data," Opt. Express **17**, 723-732 (2009).

[14] Francois X. Sillion, and Claude Puech, *Radiosity and Global Illumination*, (Morgan Kaufmann Publishers Inc., San Francisco, 1994).

[15] H.-T. Huang, C.-C. Tsai, Y.-P. Huang, J. Chen, J. Lin, and W.-C. Chang, "Phosphor conformal coating by a novel spray method for white light-emitting diodes as applied to liquid-crystal backlight module," in *proc. International Display Research Conference* (Rome, Italy, 2009) 17.5.

[16] M. Shaw and T. Goodman, "Array-based goniospectroradiometer for measurement of spectral radiant intensity and spectral total flux of light sources," Applied Optics **47**, 2637-2647 (2008).

Chapter 4

Calculation Methodology for Energy Balance Equation

Although the optical scatter properties can be characterized by BSDFs, the integration of energy balance equation (Eq. 3.14), is a subject to discuss in global illumination. In this chapter, we propose a simple but effective methodology to implement the energy integration by using discrete summation. The main purpose is to get the suitable sampling number of a considered object in the relation of Fig. 1-1. The discrete sampling grid was tested by a reference Lambertain source, which is available for practical experiment. We introduced the correlation coefficient to evaluate the predicted luminance distribution with the experimental measurement, and get a feedback to iterate the sampling number. The iterative algorithm was thus proposed to get the acceptable sampling grid. Here a commercial diffusing sheet of a LCD backlighting module was used to demonstrate the proposed algorithm.

4.1 Diffuse Scheme

Diffuse illuminations have been widely used for many fields, including projectors, liquid crystal displays, traffic signs, and luminaries. With the increasing demand of the illumination systems, the requirements for diffusing function have become more diverse, where the luminous flux is reformed into a defined radiance angles for the purpose of beam shaping, brightness homogenizing, antiglare, directionality adjustment, and so on. Meanwhile, the rapid progress in the manufacture technologies also led to many new diffusing components for various purposes. To characterize the

diffuse properties become essential for illumination design practice. However, a general and effective methodology for diffusing behavior in different area is sill insufficient.

The diffuse phenomena are mainly caused by the optical scattering. As Chapter 2 mentioned, scattering from the sheet components is caused by four mechanisms: surface topography, surface contamination, bulk index fluctuation and bulk particulates. The physical phenomena involved in the scattering are most properly described by the Maxwell's equations with appropriate boundary conditions. The modeling approaches can be conducted by either analytical or numerical solution. The analytical approaches include Kircihhoff approximation [1-4], the small perturbation method [1,3], the integral equation method [4], the small slope approximation [5,6], the facet method [7-9], and so on. Besides, the numerical methods, such as finite-difference time-domain (FDTD) [10,11] and Monte Carlo ray-tracing [12,13], have also been developed. However, only one kind of mechanisms, such as surface topography, can be considered in one physics model, where a few conditions are assumed before the calculation. Unfortunately, the appearance of objects in the real world is usually modeled as a combination of these four mechanisms, which occur simultaneously and are mutually coupled. Thus, physically based models are still used only occasionally, both because of their complexity and that the parameters are not readily available. In addition, since the commercial diffusing components are quite discrepant from the individual supplier, to analyze the complex structures is not necessary.

In this study, we present a methodology, where the measured photometric raw data sets are measured and imported into the diffuse illumination design process. First of all, we will use an experimental way to avoid directly calculating the scattering

characteristics. The measured bidirectional scatter distribution function (BSDF) is applied to characterize the scattering behavior of the diffusing feature. The approach is due to the fact that incident luminance distributions are usually provided numerically by a light-source model or measurement. To construct the outgoing field of the specific diffusing component under a certain illumination by the superposition of these photometry data is the purpose. By means of the proposed process, the required sampling points of an arbitrary diffusing component can be found out. The correlation between the simulated and measured far field radiance distribution would converge to a threshold [14]. In order to confirm the validity of the quantitative algorithm, a commercial 32-inch backlighting source associated with the diffusing sheets for liquid crystal display (LCD) was applied for the demonstration. The conclusions will show that the proposed approach can be used to accurately predict the diffused field of a broad-width source in the laminating systems.

4.2 Energy Integration

In this section, we briefly review the characteristics and terminology of the bidirectional scatter distribution function (BSDF). The associated photometric and geometric quantities in polar coordinates are illustrated in Fig. 4-1, where all the scientific symbols and names through this paper are listed in Table 4-1. In order to simplify the analysis, we restrict the discussion to the transmissive type. Of course, the study can be easily applied to the reflective type without loss of generality. First of all, we recall the bidirectional transmittance distribution function (BTDF) ρ from **Chapter 2**:

$$\rho(\theta_i,\phi_i,\theta_t,\phi_t)=\frac{dL_t(\theta_t,\phi_t)}{dE_i(\theta_i,\phi_i)}=\frac{dL_t(\theta_t,\phi_t)}{L_i(\theta_i,\phi_i)\cos\theta_i d\omega_i}\left[\frac{cd}{m^2 lx}\right], \tag{4.1}$$

where (θ_i, ϕ_i) and (θ_t, ϕ_t) represent the incident and transmitted angle of the light

transmitting the specimen. BTDF describes the radiant luminance dL_t, which is visible under the angles of observation (θ_t, ϕ_t), induced by the illuminance dE_i from a incident-side luminance L_i for an incident direction (θ_i, ϕ_i) with a solid angle $d\omega_i$. Since L_i is an available functional description, illuminance E can be decomposed into a linear combination of elementary functions. Equivalently, BTDF can be treated as the two-dimensional impulse response and completely describes the light spreading characteristics of a tested sample. The amount of light transmitted in the outgoing direction can be written as the integral of the BTDF multiplied by the incident flux from each incident direction (θ_i, ϕ_i),

$$L_t(\theta_t,\phi_t) = \int_{\Omega} \rho(\theta_i,\phi_i,\theta_t,\phi_t) L_i(\theta_i,\phi_i)\cos\theta_i d\omega_i, \tag{4.2}$$

where L_t indicates the overall luminance distribution of the transmitted light. Actually, the integration is the aforementioned energy balance equation without the emitted radiance term. Also, the integral can be expressed in a discrete way as following:

$$L_t(\theta_t,\phi_t) = \sum_j \rho_j(\theta_{i,j},\phi_{i,j},\theta_{t,j},\phi_{t,j}) L_{i,j}(\theta_{i,j},\phi_{i,j})\cos\theta_{i,j} \cdot rect(\theta_{i,j},\phi_{i,j}), \tag{4.3}$$

where the rectangular function rect(ω_i.) indicates the solid angle around the specific incident angle ($\theta_{i,j}$,$\phi_{i,j}$). Based on the linear composition of every *j-th* components, the hemispherical luminance distributions over the transmission side can be solved accordingly.

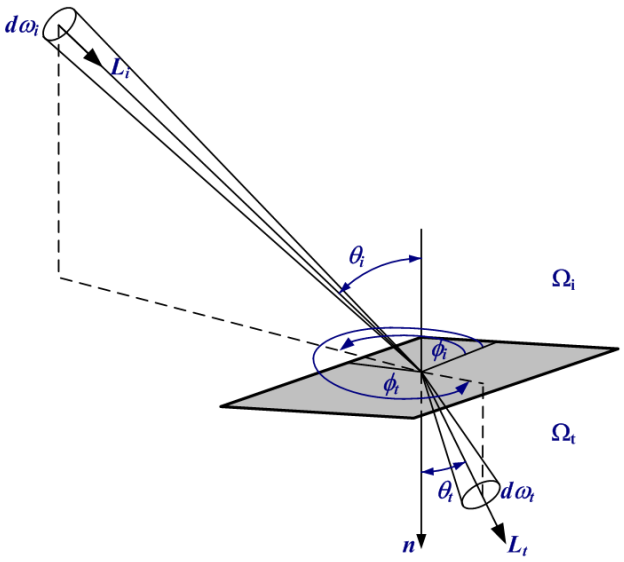

Fig. 4-1 Photometric and geometric quantities in the polar coordinate

Table 4-1. Nomenclature

Capital letters		*Greek letters*		*Subscripts*	
L	luminance (cd/m^2)	***ω, Ω***	solid angle (sr)	***i***	incident
E	illuminance (lx)	***ε***	error	***t***	transmitted
CC	correlation coefficient	***θ, ϕ***	polar coordinates	***c***	calculated
W	weighting factor	***τ***	transmittance	***e***	experimental
ρ	bidirectional transmission distribution function (sr^{-1})	***Φ***	light flux	***j, m***	count
		δ	delta function	***r***	reference

4.3 Iterative Algorithm

The proposed procedure for modeling a diffusing specimen is shown in Fig. 4-4. The conception is to find the acceptable sampling points of the diffusing component through comparing the outgoing fields by our construction and the reference measurement. The algorithm is started with the aforementioned BTDF measurement. Based on the measured BTDFs, a rotational superposition was performed to

implement the rotationally-constructed BTDFs (R-BTDFs). A rotationally symmetric source, that is practically available, illuminated on the sample for the purpose of calculation reference, and the luminance weights at different inclinations of the reference source were introduced into the R-BDTFs to calculate the outgoing field. After that, we will introduce a merit value (correlation coefficient) to compare the simulated far field luminance with the measured results. The correlation coefficient provides a feedback to correct the sampling point until the merit value converges to an acceptable value. In the following, the sample in Fig 4-3 (b) will be taken for the demonstration of the algorithm.

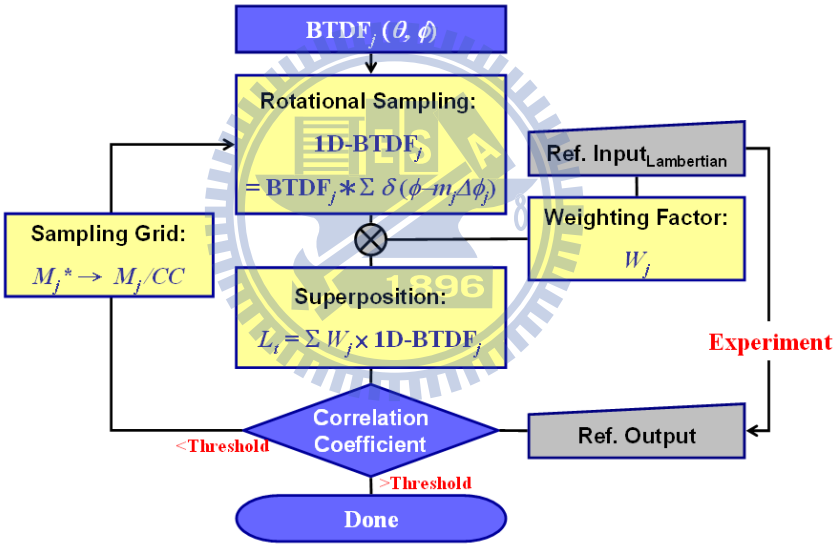

Fig. 4-2. Modeling procedure for a commercially available diffusing

4.3.1 Rotational Construction by BTDFs

Because the procedure is based on calculating the transmitted field by constructing the BTDFs, the rotational sampling of the BTDF is performed first. A rotationally symmetric field is assumed to illuminate the specimen. Therefore, the dependence along the azimuthal direction can be degenerated by taking convolution

between the measured BTDFs ρ_j, which is the *j-th* inclination set as shown in Fig. 4-2, and a comb function along the azimuthal direction:

$$\begin{aligned}\rho_j^{\,R}(\theta_t,\phi_t) &= \rho_j(\theta_t,\phi_t) * \sum_{m_j=0}^{M_j} \delta(\theta_t - j\Delta\theta, \phi_t - m_j\Delta\phi_j) \\ &= \sum_{m_j=0}^{M_j} \rho_j(\theta_t - j\Delta\theta, \phi_t - m_j\Delta\phi_j),\end{aligned} \tag{4.4}$$

where j and $\Delta\theta$ represent the shifts along θ direction with the interval $\Delta\theta$. m_j and $\Delta\phi_j$ indicate the shifts along ϕ direction of the *j-th* inclination. ρ_j^R is the *j-th* rotationally-constructed BTDF (R-BTDF). In our case, the width of the horizontal band $\Delta\theta$ is 10 degrees, which is mentioned in the measured results in section *2.2*. Here the sampling number M_j, which means 2π is equally divided into M_j divisions, is increased with the outer band, so the sampling interval $\Delta\phi_j$ is varied with different j. Fig. 4-5 shows an numerical calculation of convolution of the 40°-inclination (j=4 the fourth ring) BTDF. Because of the nature of the integrated solid angle, the arrangement of M_j should be directly proportional to the zonal constant [23], which is a convenient factor to calculate the luminous flux emitted into a narrow band and multiplying the summation by a solid angle factor. After a number of straight manipulations, eight donut-like R-BTDF ρ_j^R can be obtained accordingly.

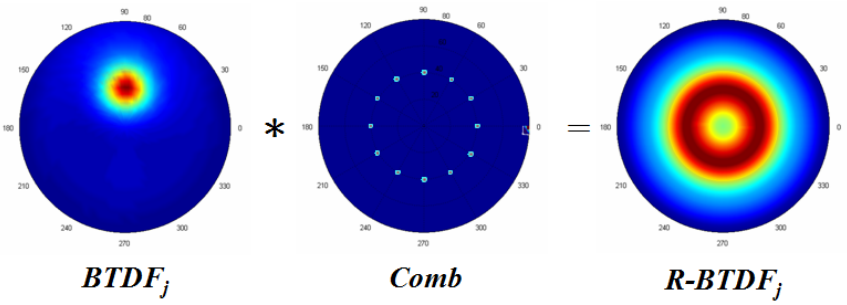

Fig. 4-5 The convolution of 40°-inclination

The scattering from a diffusing sheet can be treated as the radiant flux emitted from a secondary flat source. The zonal constant integration technique is a convenient method to numerically integrate the radiation pattern of the light source into a value of the luminous flux. It calculates the luminous flux emitted into a narrow band and multiplying the summation by a solid angle factor, called the zonal constant. We apply this factor into our algorithm, where the sampling point of the angular divisions M_j is proportional to the zonal constant.

The value of zonal constant $C_z(\theta_j)$ can be derived by calculating the surface area for one horizontal band on the surface of the hemisphere and converting the surface area value into the subtended solid angle. Fig. 4-6 (a) schematically shows the surface area of the *j-th* horizontal band. If the hemisphere is equally divided into J vertical divisions, the polar angular increment $\Delta\theta$ is equal to $\pi/2J$. Thus, the zonal constant C_z is equal to the simplified solid angles of the horizontal band:

$$C_z(\theta_j) = 2\pi \cdot \frac{\pi}{2J} \sin\theta_j = 2\pi\Delta\theta \sin\theta_j. \tag{5}$$

However, the continuous solid angle ω of the horizontal band can be derived as

$$\omega = 2\pi \int_{\theta_j - \Delta\theta/2}^{\theta_j + \Delta\theta/2} \sin\theta d\theta = 4\pi \sin\left(\frac{\Delta\theta}{2}\right) \sin\theta_j. \tag{6}$$

Comparing the zonal constant with the exact solid angle of the horizontal segment yields an error as:

$$\varepsilon = \frac{\Delta\theta - 2\sin\left(\frac{\Delta\theta}{2}\right)}{2\sin\left(\frac{\Delta\theta}{2}\right)} \times 100\%. \tag{7}$$

In our case, the C_z approximation gives an error about 0.25% when the width of the horizontal band is 10 degrees. Fig. 4-6 (b) shows the numerical comparison between the zonal constant and the continuous solid angle. The zonal constants represent the relation of the solid angles on different horizontal band. To make the reconstructed

arrangement of impulse response in a homogeneous distribution, M_j should be directly proportional to the zonal constant.

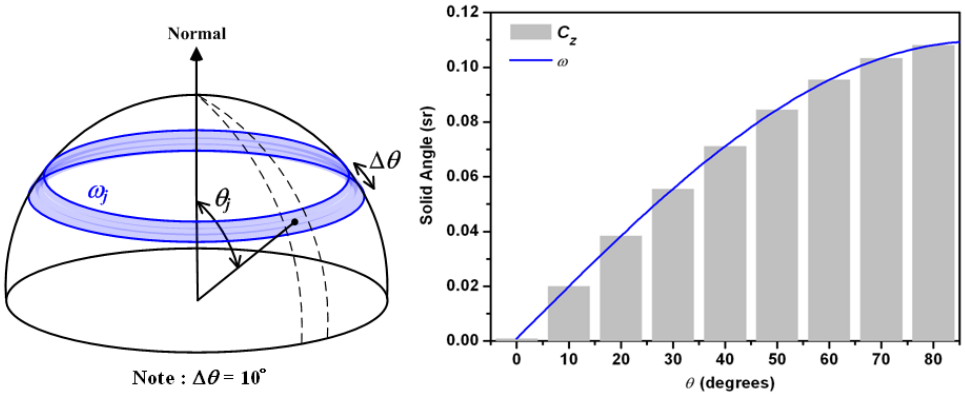

(a) (b)

Fig. 4-6 (a) The schematic illustration of the horizontal band. (b) Comparison between exact solid angle and the zonal constant of horizontal band.

4.3.2 Weighting & Superposition of R-BTDFs

A rotationally symmetric reference light source is essential in the calibration of the algorithm. Usually, a Lambertian field is adopted due to its uniform luminance and easily offered by the conventional sources, which include the surfaces of fluorescent lamps or the light diffused by a thick diffusing plate. In our case, the measurement is performed by the setup where the light emitted from a tungsten lamp passes through a diffusion plate and Lambertian emission is measured by conoscopic system. In order to calculate the transmitted field under the reference illumination by BTDFs, each R-BTDF (j=0~7) is weighted by the factor W_j in accordance with the Lambertian reference source subject to the corresponding inclinations. The weights W_j is the luminance at *j-th* inclination θ_j of the reference incident function $L_{i,r}$ over the value in normal direction θ_0 under a constant azimuth ϕ_0.

$$W_{i,j} = \frac{L_{i,r}(\theta_j, \phi_0)}{L_{i,r}(\theta_0, \phi_0)} = \left. \frac{L_{i,r}(\theta, \phi) \cdot \delta(\theta - j\Delta\theta, \phi - \phi_0)}{L_{i,r}(\theta, \phi) \cdot \delta(\theta - \theta_0, \phi - \phi_0)} \right|_{\theta_0 = 0°, \phi_0 = 90°} . \tag{4.5}$$

The scattering light field is determined by the superposition of the eight weighted R-BTDFs. Normalized luminance distribution of the transmitted light can be represented as:

$$\begin{aligned} L_t(\theta_t, \phi_t) &= A \cdot \sum_{j=0}^{J} W_{i,j} \cos\theta_{i,j} \cdot \rho_j{}^R(\theta_t, \phi_t) \\ &= A \cdot \sum_{j=0}^{J} \sum_{m_j=0}^{M_j} W_{i,j} \cos\theta_{i,j} \cdot \rho_j(\theta_t - j\Delta\theta, \phi_t - m_j d_j), \end{aligned} \tag{4.6}$$

where A is the normalized coefficient, and calculated by

$$A^{-1} = \left. \sum_{j=0}^{J} \sum_{m_j=0}^{M_j} W_{i,j} \cos\theta_{i,j} \cdot q_j(\theta_t - j\Delta\theta, \phi_t - m_j d_j) \right|_{\theta=0, \phi=0} .$$

Similar to Eq. (4.3), Eq. (4.6) has an identical form expect the weighting factors W_j are introduced by the reference Lambertian source. Here the cosine term is a tilt factor between the light source and the illuminated plane. Fig. 4-7 exhibits the individual R-BTDFs and their superposition results, which means the constructed outgoing distribution. Although the normalized luminance distribution through the diffusing specimen from a Lambertian source is obtained, however, the accuracy of the calculation highly depends on the number of discrete sampling component. Consequently, an additional merit index is required to gauge the accuracy of the proposed algorithm. The amount of sampling number is sequentially increased and correlated with its measurement. In the absence of continuity, the algorithm would obtain the discrete points for BTDF superposition and keep the outgoing field in certain accuracy.

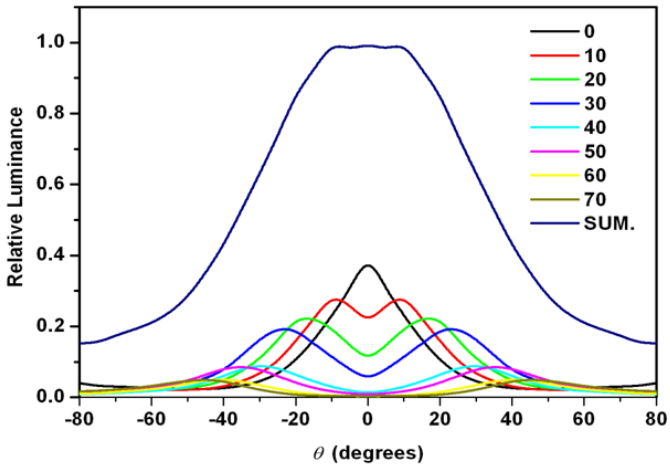

Fig. 4-7 The cross-section of individual 1D-BTDF and summation under Lambertian illumination.

4.3.3 Correlation Coefficient

Correlation coefficient is a merit value to gauge the accuracy of the numerical construction and served as a feedback for correcting the sampling points. Thus, we correlate the calculated field with its measurement, which are both the response of the reference Lambertian source. The correlation coefficient *CC* is defined as:

$$CC = \frac{\sum_{\theta}\sum_{\phi}\left[L_c(\theta,\phi)-\bar{L}_c\right]\left[L_e(\theta,\phi)-\bar{L}_e\right]}{\sqrt{\sum_{\theta}\sum_{\phi}\left[L_c(\theta,\phi)-\bar{L}_c\right]^2\sum_{\theta}\sum_{\phi}\left[L_e(\theta,\phi)-\bar{L}_e\right]^2}}, \tag{4.7}$$

where L_c and L_e are the normalized luminance distributions of the calculation and its measurement, respectively. $\bar{L}_c$ and $\bar{L}_e$ are the mean values of both corresponding datasets. If *CC* is below a threshold value T, it means the calculated field has a certain amount of discrepancy with the real one. Because the deviation is mainly due to the finite sampling points in the superposition, we would increase the sampling number ΣM_j by an incremental rate $\Sigma M_j \times CC^{-1}$ until *CC* is above the desirable threshold value. Eventually, the amount of the angular sampling ΣM_j along the azimuthal direction can

converge to an acceptable value. In case of the commercially available diffuser in the Fig. 3(b), the correlation coefficient can be achieved upon 98% as the sampling number exceeds 357. Certainly, the sampling number is related to the optical complexity and dependent on the optical features by case. Because the retrieved output field is calculated by the superposition of finite number of BTDFs, the finite sampling points easily cause the discrete calculated fields or incorrect results. The profiles of BTDFs directly affect the required sampling number. The broader BTDF profile requires less sampling points, and the distribution is related to the structure of the diffusing sheets, as we mentioned in section 2.2.

4.4. Evaluation

Aforementioned procedure is employed to determine the sampling grid of the BTDFs for calculating the optical response of the specimen, so we are able to directly apply the results to calculate the transmitted luminance distribution from assigned illuminating sources L_i. The weighting function $W(j,m)$ corresponding to the known sampling grid, can be obtained by:

$$W_{j,m_j} = \frac{L_i(\theta_j, \phi_{m_j})}{L_i(\theta_0, \phi_0)} = \left. \frac{L_i(\theta,\phi)\cdot\delta(\theta - j\Delta\theta, \phi - m_j\Delta\phi_j)}{L_i(\theta,\phi)\cdot\delta(\theta-\theta_0, \phi-\phi_0)} \right|_{\theta_0=0°,\phi_0=90°}. \tag{4.8}$$

Thus, the transmitted distribution function can be calculated by two-dimensional superposition of the BTDFs multiplied by the corresponding weight function,

$$L_t(\theta_t, \phi_t) = \sum_{j}^{J} \sum_{m_j}^{M_j} W_{j,m_j} \cdot \cos\theta_{i,j} \cdot \rho_j(\theta_t - j\Delta\theta, \phi_t - m_j\Delta\phi_j). \tag{4.9}$$

In addition to the normalized luminance distribution, the absolute value is able to be calibrated by the transmittance $\tau(\theta)$ as following:

$$\tau(\theta_i) = \frac{\Phi_t}{\Phi_i(\theta_i)} = \int_{\Omega_t} \frac{L_t(\omega_t)}{E_i(\omega_i)} \cos\theta_t d\omega_t = \int_{\Omega_t} \rho(\omega_i, \omega_t) \cos\theta_t d\omega_t, \tag{10}$$

where the Φ_t and Φ_i are the overall luminous flux from the incident and transmitted sides of the diffusing sheet. In most case of diffusing sheets, the transmittances $\tau(\theta_i)$ are a constant with respect to different incident angles, so the absolute value of the transmittance can be applied on light sources with variant angular distributions. The transmittances can correct the normalized luminance distribution to absolute luminance value. The calculated result for the sample we mentioned is shown in Fig. 4.8(a), where the transmitted luminance distribution was from a commercially available 32”-TV backlighting source. Comparing with the experimental results in Fig 4.8(b), the close agreement with the measurement (*CC* =98.6%) demonstrates the validity of the proposed training process and corresponding diffusing model. The negligible deviations at large angles were mainly resulted from the measurement errors attributed by the conoscope distortion.

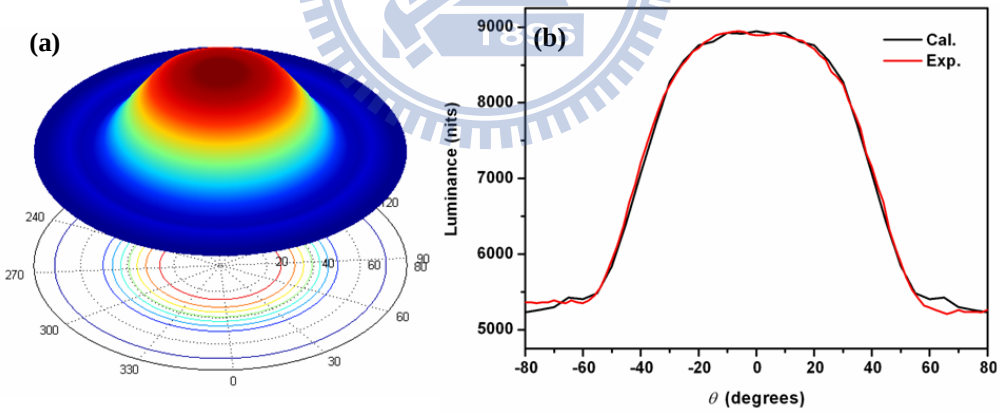

Fig. 4-8 Angular luminance distribution transmitted through the diffuser from a 32-inch backlighting source by (a) calculation, and (b) comparison of the cross-sections at ϕ = 0 and 360 degree, where the *CC* between two curves is 98.6%.

4.5 Summary

A simple and effective algorithm to model the scattering characteristics of the diffuser is proposed and demonstrated. The major advantage of this study lies in that there is

no need to formulate the complex physical mechanism of the scattering in a microscopic viewpoint. Instead, as long as a backlighting source (Cold Cathode Fluorescent Lamp or Light Emitting Diode) is available, proposed semi-quantitative algorithm can predict the optical radiance and efficiency with high precision without expense of computational time. The proposed algorithm is based on eight measured BSDFs and a reference Lambertian light source. Additional correlation coefficient is employed to evaluate the model accuracy and eventually converge to a stable sampling parameter. Thus, this modeling scheme only needs the BTDFs and the sampling parameter M_j to characterize one diffusing sheet and it is convenient for designers or factories to build a diffuser database. We successfully demonstrate the validity by using a general backlight source, where calculated emergent luminance distribution is 98.6% close to the measurement. In most case, *CC* can achieve the value larger than 98%. The algorithm provides a relatively effective way for diffusing simulation, and is useful for the lighting development in display or luminance application.

4.6 References

[1] M. Nieto-Vesperinas, *Scattering and Diffraction in Physical Optics* (Wiley, New York, 1991).

[2] L. Tsang, J. A. Kong and K. –H. Ding, *Scattering of Electromagnetic Waves, Theories and Applications* (Wiley, New York, 2000).

[3] L. Tsang, and J. A. Kong, Scattering of Electromagnetic Waves, Advanced Topiics s (Wiley, New York, 2001).

[4] A. K. Fung, Microwave Scattering and Emission Models and Their Applications (Artech House, Boston, 1994).

[5] A. Voronovich, “Small-slope approximation for electromagnetic wave scattering at a rough interface of two dielectric half-spaces,” Wave in Random Media **4**, 337-367 (1994).

[6] A. Voronovich, *Wave Scattering from Rough Surfaces, 2nd Edition*

(Springer-Verlag, Berlin Heidelberg , 1994).

[7] K. E. Torrance and E. M. Sparrow, “Theory for off-specular reflection from roughened surface,” J. Opt. Soc. Am. **57**, 1105-1114 (1967).

[8] B. van Ginneken, M. Staveridi and J. J. Koendrik, “Diffuse and specular reflectance from rough surface,” Appl. Opt. **37**, 130-139 (1998).

[9] K. Tang and R. O. Buckius, “A statistical model of wave scattering from random rough surfaces,” Int. J. Heat Mass Transfer **44**, 4095-4073 (2001).

[10] L. Tsang, J. A. Kong, K, -H. Ding and C. O. Ao, *Scattering of Electromagnetic Waves, Numerical Simulations* (Wiley, New York, 2000).

[11] F. D. Hastings, J. B. Schneider, and S. L. Broschat, “A Monte Carlo FDTD technique for rough surface scattering,” IEEE Trans. Antennas Propag. **43**, 1183-1191 (1995).

[12] N. Garcia and E. Stoll, “Monte Carlo calculation for electromagnetic-wave scattering from random rough Surfaces,” Pgys. Rev. Lett. **52**, 1798-1801 (1984).

[13] K. Tang, R. Dimenna and R. Buckius, “Regions of validity of the geometric optics approximation for angular scattering from very rough surface,” Int. Heat J. Mass Transfer **40**, 49-59 (1997).

[14] E. Kreyszig, *Introductory Mathematical Statistics,* (Wiley, New York, 1970)

[15] M. W. Hodapp, *”Applications for High-Brightness Light-Emitting Diodes”* in *Semiconductors and Semimetals Vol. 48*, G. B. Stringfellow and M. G. Craford ed., (Academic Press, San Diego, 1997) Semiconductors and Semimetals Vol. 48, Chap. 6, p. 227.

Chapter 5

Application:
Planer Lighting by Remote Phosphor Sheet

5.1 Blue LEDs Array with Remote Phosphor Sheet

In this study, we proposed a blue light excited planar lighting (BLPL) system, which is an alternative LEDs-based direct-emitting planar scheme. Fig. 5-1(b) shows the structure of BLPL, which consists of a blue LEDs array and a YAG-phosphor film. Here the YAG phosphor is coated on a remote substrate. The YAG-phosphor layer is simultaneously functioned as the diffuser film and wavelength down converter to achieve an ultra-slim LCD backlight application [4].

Fig. 5-1. Scheme of (a) conventional direct-emitting backlight using white LEDs and (b) BLPL system.

The light emitting mechanism of BLPL system includes wavelength-converting process and scattering by the flat YAG-phosphor particle, as illustrated in Fig. 5-2. Unlike the conventional phosphor-converted LEDs, the YAG-phosphor in BLPL system is coated on an external substrate by the roll-to-roll coating process [5]. The YAG-phosphor layer here acts as a diffuser film and a wavelength-converter at the same time. As the blue light from blue LED chips irradiate the YAG-phosphor layer,

portion of the incident blue light will be diffused with high diverging angle, whereas the other part of the incident blue light will be converted to a certain bandwidth, as shown in Fig. 5-3. For the BLPL system, flat phosphor layer redistributes lights and converts the original point light sources to the planar light source. Thus, the proposed optical setup could perform uniform lighting and reduce module thickness of backlight systems.

Because light-emitting mechanism of BLPL involves both spectral and spatial conversion, the traditional ray-tracing computational tools are insufficient to completely treat the underlying physics. Based on the bidirectional photometric measurable data, this paper proposed a methodology to model, analyze and optimize the BLPL system. Finally, a small-size prototype will be demonstrated to validate the model.

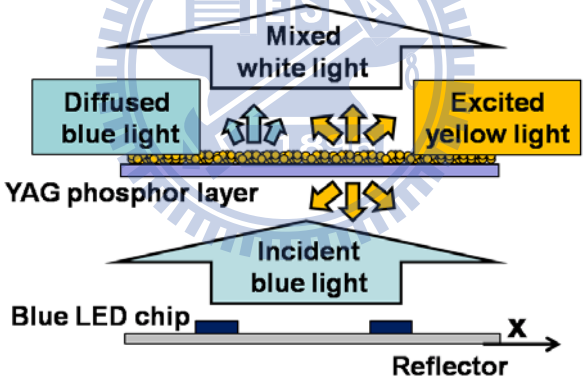

Fig. 5-2 The scheme of the BLPL system with light-emitting mechanism.

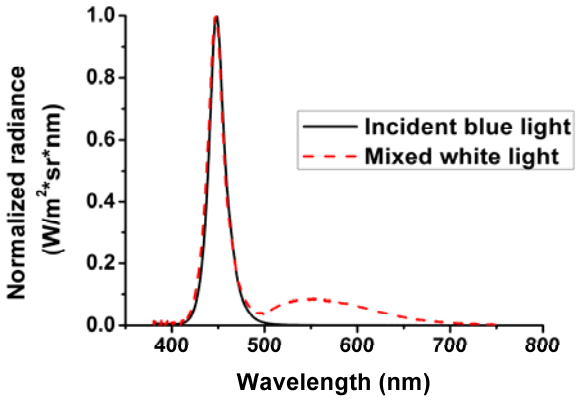

Fig. 5-3 Spectrum of the incident blue light and the mixed white light.

5.2 Optical Characteristics of YAG-phosphor

The optical properties of YAG-phosphor layer could be characterized by the measured bidirectional transmittance distribution functions (BTDFs), which is defined as [6-8]:

$$BTDF(\theta_i,\phi_i,\theta_t,\phi_t)=\frac{L_t(\theta_t,\phi_t)}{E_i(\theta_i,\phi_i)}, \tag{5.1}$$

where E_i is the illuminance on the sample plane due to the incident light, L_t is the luminance of transmitted light from the sample surface. Here the incident and emit angles are represented by the polar coordinates (θ_i,ϕ_i) and (θ_t,ϕ_t), respectively. Since the scattering characteristics of YAG-phosphor layer caused by the randomly distributed phosphor are rotationally symmetric. The measurement and data processing of BTDFs can be simplified by merely considering the variance of polar angle θ_t with a fixed azimuthal angle ϕ_t.

BTDFs represent the angular spread function of the diffusing specimen, which have a variety of optical features due to various manufacturers' recipes about the refractive index, the size of scattering particles, the density of the phosphor distribution, and so on. The major advantage of this study lies in that there is no need to formulate the complex physical mechanism of the phosphor scattering in a microscopic viewpoint. Instead, as long as the LED chip is available, the proposed characterizing method can assist the simulation of the optical radiance and the efficiency.

Differing from the traditional definition of the BTDFs, the BTDFs we defined can represent the scattered light and the emitted light by the spectrally filtered measurements. Owing to the two kinds of optical mechanisms under the blue light illumination, the diffused blue light and the emitted yellow light were measured

separately. Fig. 5-4 (a) and (b) show the BTDF measured results of the YAG-phosphor. The angular distribution of the excited yellow light is close to lambertian and has a wider full width at half maximum (FWHM) than the diffused blue light. By these two measured BTDF results, the YAG-phosphor layer could be characterized to develop the BLPL model.

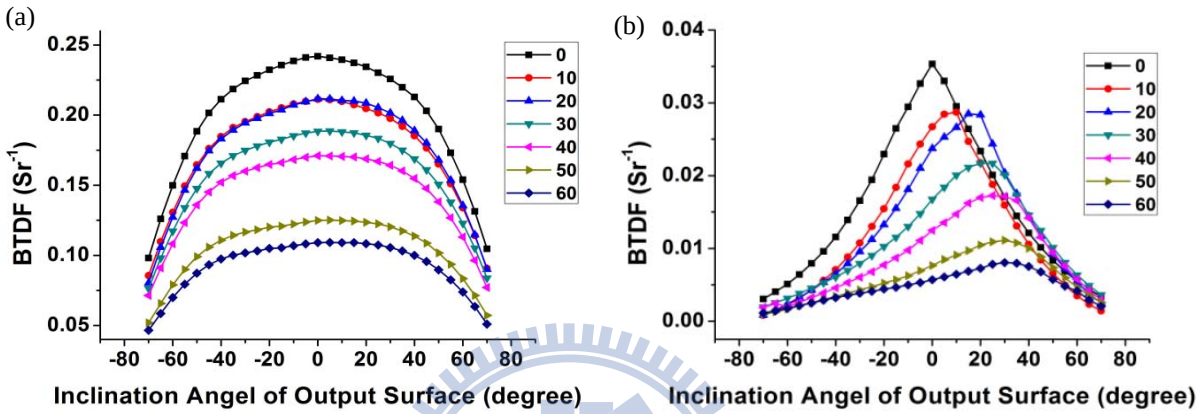

Fig. 5-4 The measured BTDF of (a) the emitted yellow-light radiance and (b) the scattered blue-light radiance

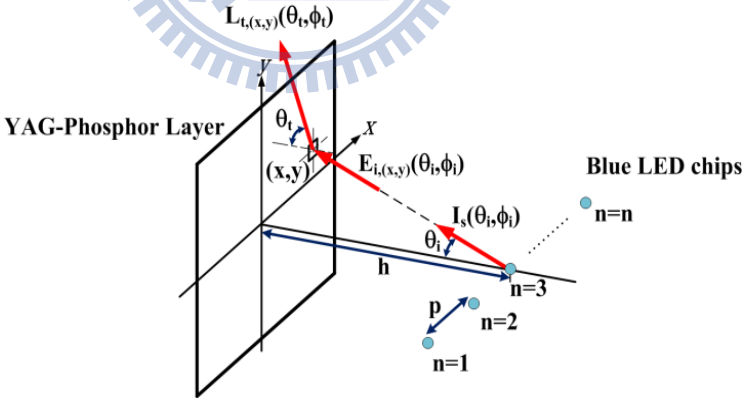

Fig. 5-5 Scheme of theoretical calculation.

5.3 Theoretical Calculation

By using the characterizations of the YAG-phosphor layer, a theoretical model was developed to calculate the transmitted luminance distribution of BLPL system. First of all, the four major parameters of the BLPL configuration should be obtained for the

theoretical calculation: (1) the BTDF of the YAG-phosphor layer, (2) the intensity distribution I_s of the LED chips, (3) the distance h between LED chips and YAG-phosphor layer, and (4) the interval p of the LED arrangement. Through the definition of radiometry, the illuminance E illuminating the YAG phosphor layer at the point (x, y) from the incident direction (θ_i, ϕ_i) of single blue LED can be calculated by

$$E_{(x,y)}(\theta_i,\phi_i)=\frac{I_s(\theta_i,\phi_i)\cdot\cos^3\theta_i}{h}. \tag{5.2}$$

Here the geometric relation is schematically shown in Fig. 5-5. Then, the transmitted luminance distribution L_t from the YAG-phosphor layer at point (x, y) can be transferred by the BTDFs

$$\begin{aligned} L_{t,(x,y)}(\theta_t,\phi_t) &= \int_{\Omega_i} BTDF_{(x,y)}(\theta_i,\phi_i,\theta_t,\phi_t)\cdot E_{i,(x,y)}(\theta_i,\phi_i)d\omega_i \\ &= \int_{\Omega_i} BTDF_{(x,y)}(\theta_i,\phi_i,\theta_t,\phi_t)\cdot\frac{I_s(\theta_i,\phi_i)\cdot\cos^3\theta_i}{h}d\omega_i. \end{aligned} \tag{5.3}$$

Finally, the total radiating luminance L_{output} from the YAG-phosphor layer by LED-array illumination can be calculated by the convolution between the single-LED luminance distribution $L_{t,(x,y)}$ and a two-dimensional comb function

$$\begin{aligned} &L_{output}(\theta_t,\phi_t;x,y) \\ &=\sum_n\sum_m\left[\int_{\Omega_i} BTDF_{(x,y)}(\theta_i,\phi_i,\theta_t,\phi_t)\cdot\frac{I_s(\theta_i,\phi_i)\cdot\cos^3\theta_i}{h}d\omega_i * \delta(x-np,y-mp)\right], \end{aligned} \tag{5.4}$$

here the counting number n and m indicate the *n-th* and *m-th* LED along x and y direction, respectively. In this case, the summation and integration were performed by Monte Carlo simulation [9]. In addition to the transmitted luminance distribution, the recycled light which is multi-reflected by the YAG-phosphor film and the bottom reflector can be identically calculated by the bidirectional reflection distribution functions (BRDFs).

5.4 Simulation

For the LED backlit use, a 5x5 blue LED chips array was placed above a reflector and covered with the YAG-phosphor layer, as shown in Fig. 5-6. We import the measured BSDFs into the commercial software LightTools ™ to accomplish the influence of YAG-phosphor on the whole BLPL system. In order to keep the uniformity and luminance as the first merit, the module gap (h) and the interval of blue LED chips (p) were modulated from 4 to 20 mm. Here the luminance uniformity is defined as

$$Uniformity = \left. \frac{L_{output,\min}}{L_{output,\max}} \right|_{\theta_t = 0}, \tag{5.5}$$

which is the luminance ratio of the positions with the minimum luminance and the maximum luminance at the normal viewing direction. The simulated luminance uniformity is shown in Fig. 5-7 in comparison with a conventional white LED direct-emitting backlit (covered by diffuser plate).

It is found that the operating region is much wider in BLPL system than the conventional backlit due to BLPL structure includes a strong scattering function conducted by YAG-Phosphor layer in the optical path. Even without additional diffuser or diffusing plate, high uniformity is able to be achieved under ultra-slim configuration. As shown in Fig. 8, as spacing between the LED chip and diffusing structure is reduced to 10 mm (cross line (b) and (e) in Fig. 5-7), the optimized light-redistributed mechanism on the flat YAG-phosphor layer makes BLPL system achieved 82% uniformity associated with 10-mm LED interval, whereas the conventional white LED backlight with 20% uniformity with the identical LED interval, the results exhibit the advantage of remote phosphor for uniformity issue in large-area backlit applications.

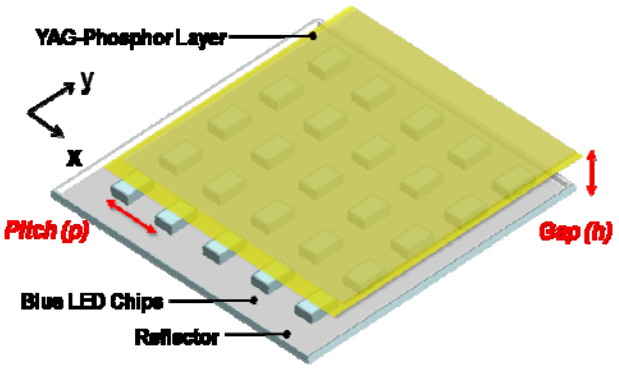

Fig. 5-6 The scheme of the BLPL structure for simulation

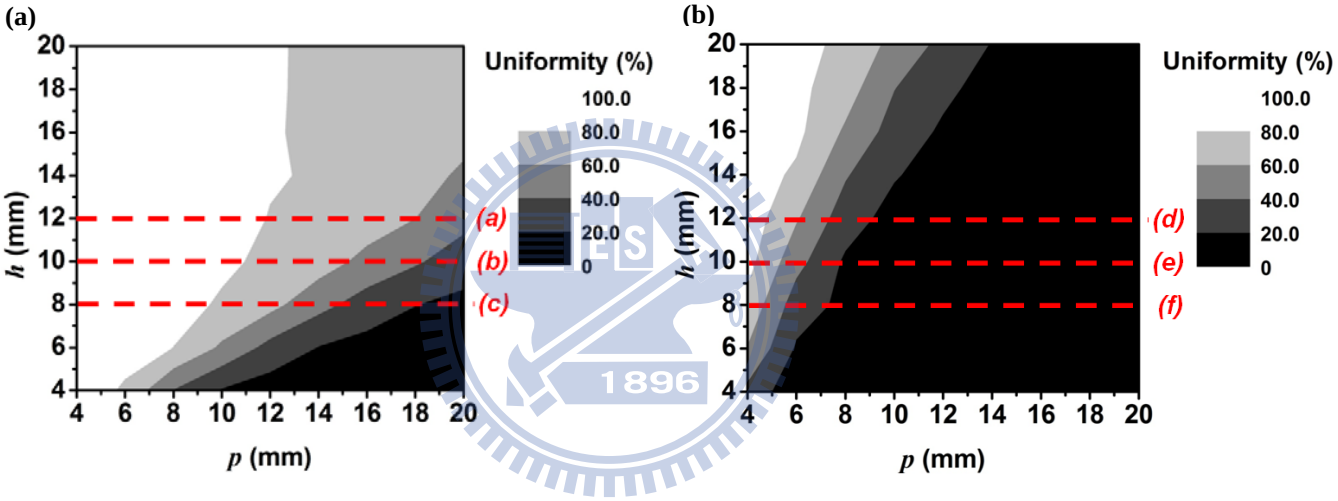

Fig. 5-7 The simulated uniformity of (a) the BLPL system and (b) LEDs array with varied LED pitch and system gap.

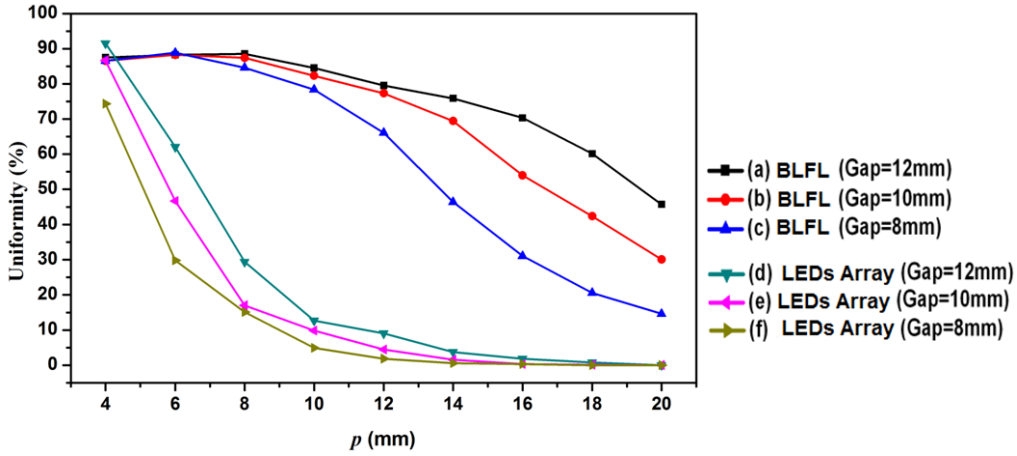

Fig. 5-8 The comparison of the uniformity between the BLFL and the LEDs array

Off-axis color deviation, which is a major optical issue of a backlight system, was considered in the BLPL system. Based on the uniformity optimization, the 10-mm mixing gap was chosen as the appropriate parameters for the slim backlight design. Thus, the chromaticity at the center of the simulation model (as shown in Fig. 5-9) was obtained, and the color differences ($\Delta u'$, $\Delta v'$) versus different viewing inclinations θ were evaluated (the chromaticity quantities are introduced in Appendix). Fig. 10 represents the color deviations $\Delta u'v'$ of the 0°-30° and 0°-60° viewing inclinations, respectively. According to the results, the LED arrangements with 8-10 mm interval have relatively low color difference.

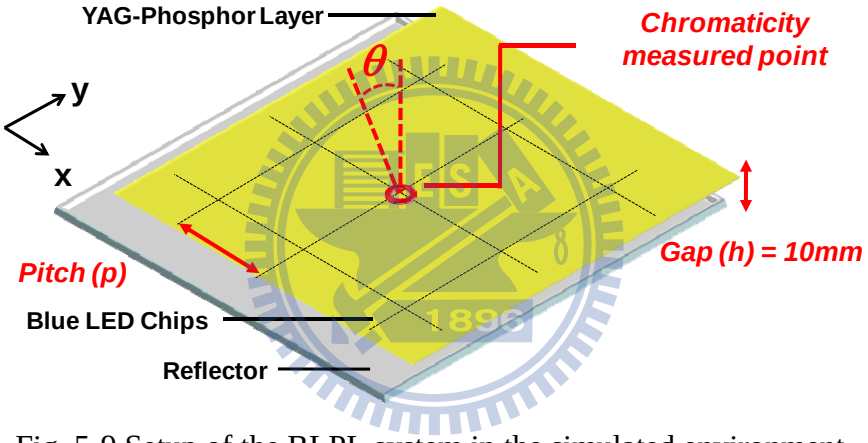

Fig. 5-9 Setup of the BLPL system in the simulated environment.

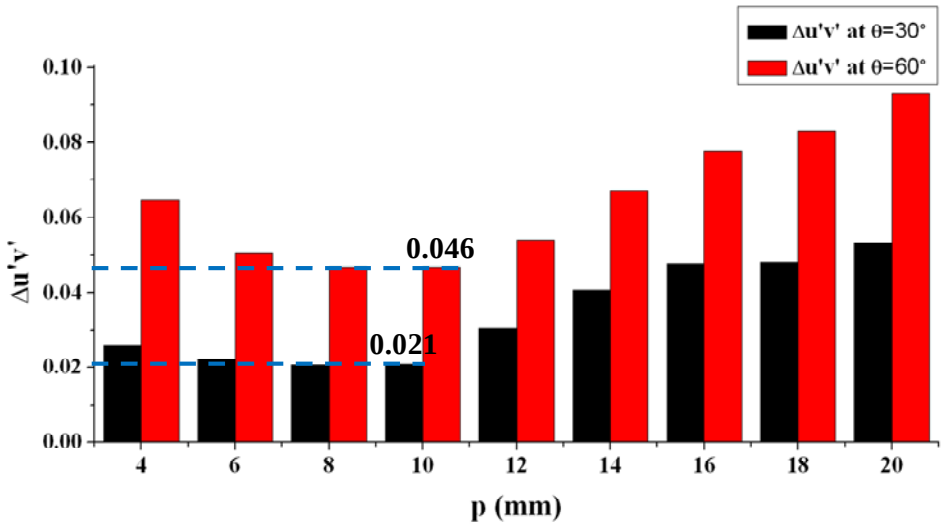

Fig. 5-10 The color difference ($\Delta u'v'$) with a fixed module gap (10mm) and varied LED pitches (4-20mm).

From the previous simulation, the 10-mm light mixing space with 8-10 mm LED interval were chosen as the appropriate geometrical parameters of the BLPL system for the purpose of the slim backlight design. However, the radiated blue light has a relatively narrower angular distribution than the radiated yellow light. Therefore, the BLFL system exhibits a yellowish phenomenon in large viewing direction. This issue can be suppressed by using the commercial optical films with a lenticular configuration.

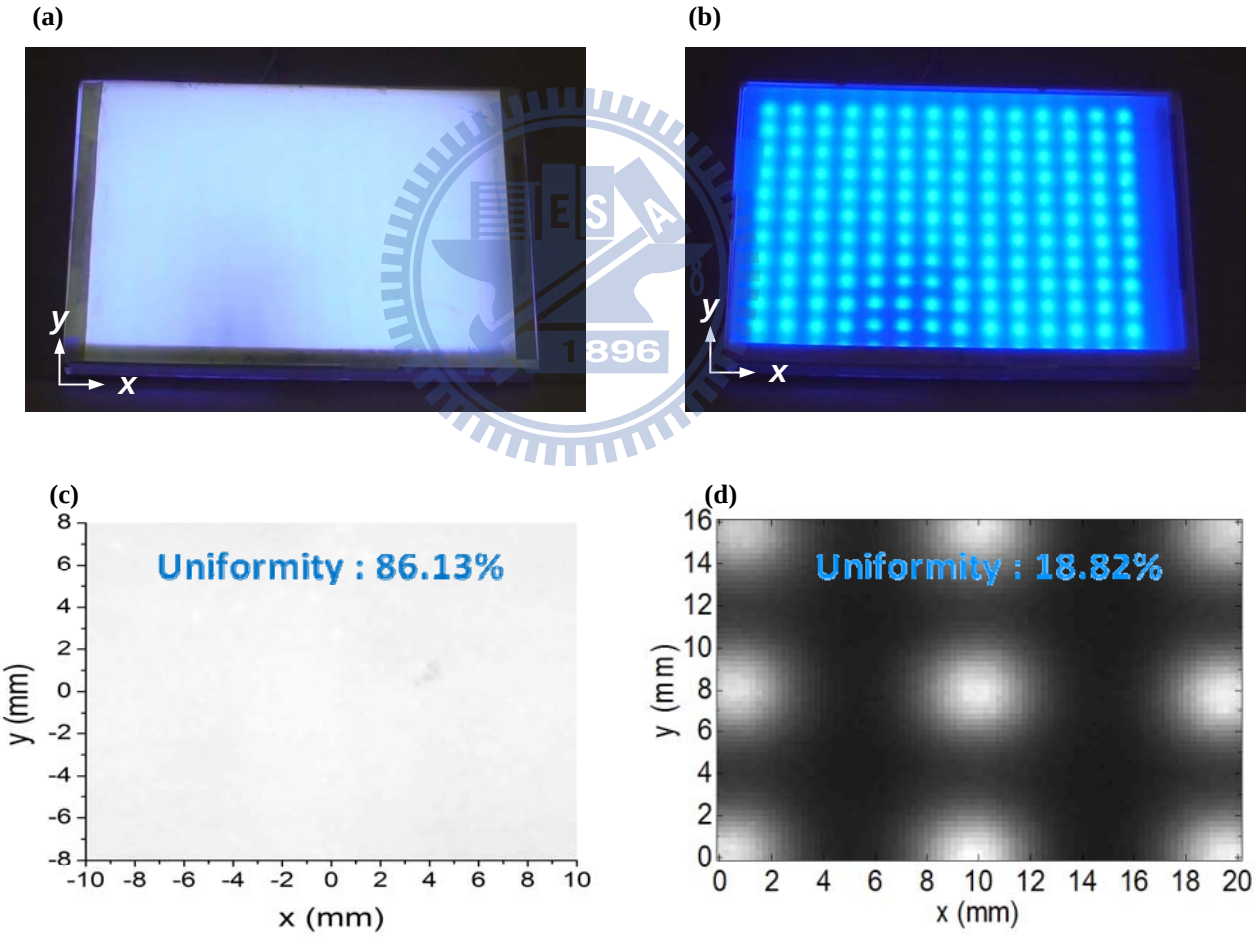

Fig. 5-11 The experimental results of (a) (c) the BLPL system and (b) (d) the direct LEDs array

5. 5 Experiment

Based on the BTDFs of YAG-Phosphor layer and optimized LED layout, a 7-inch slim BLPL system was demonstrated. Compared with a conventional backlight with a commercial diffuser (80% Haze) under the same LED interval and mixing space, the experimental results are shown in Fig. 5-11. The emitted luminance of BLPL system achieved 9800 nits and the 86% uniformity, whereas the conventional backlight had only 5600 nits and 18% uniformity. Thus, BLPL system indeed showed the potential for fabricating the ultra-slim backlight system for the large-sized LCD-TV applications.

5.6 Summary

The optical properties of the blue light excited planar lighting (BLPL) system had been discussed in this paper. In BLPL system, the YAG-phosphor acts as a diffuser film and the wavelength converter simultaneously. Thus the BLPL system generated flat lighting and performed higher uniformity than the conventional direct-emitting backlight with white LEDs. However, such specific optical property makes BLPL system hard to be simulated by conventional simulation software. By using the characterization of the YAG-phosphor layer, a methodology for the purpose of modeling the BLPL system was proposed. According, a prototype slim format BLPL system had been demonstrated. The small-sized BLPL system achieved 86% uniformity and 9800nits with 10-mm backlight module thickness and without using any diffuser film or plate, while the conventional backlight system had only 20% uniformity and 5600nits with the same backlight module thickness. Consequently, BLPL system is indeed the potential technology for developing the future backlight system with high brightness and ultra-slim module thickness.

5.7 References

[1] Munisamy Anandan, “Progress of LED backlights for LCDs,” Journal of the SID **16/2**, pp. 287-310 (2008).

[2] D. Feng, Y. Yan, X.Yang G. Jin and S. Fan, “Novel Integrated Light-Guide Plates for Liquid Crystal Display Backlight,” J. Opt. A: Pure Appl. Opt., vol. **7**, 111-117 (2005).

[3] Y.-H. Lu and C.-H. Tien, “Novel Direct-LED-Backlight Unit Using Grooved Hexagonal Light-Guide Plate,” SID Int. Symp. Digest Tech. Papers 37(2), 1513-1516 (2006).

[4] Y. Ito, T. Tsukahara, S. Masuda, T. Yoshida, N. Nada, T. Igarashi, T. Kusunoki, and J. Ohsako, “Optical Design of Phosphor Sheet Structure in LED Backlight System,” SID Int. Symp. Digest Tech. Papers 39(2), 866-869 (2008).

[5] H.-T. Huang, C.-H. Hung, Y.-P. Huang, C.-H. Tien, C.-C. Tsai, and H.-P. D. Shieh, “UV Excited Flat Lighting (UFL) System for LCD-TV Backlight Application,” SID Int. Symp. Digest Tech. Papers 39(2), 862-865 (2008).

[6] Chung-Hao Tien and Chien-Hsiang Hung, “An iterative model of diffuse illumination from bidirectional photometric data,“ Optics Express **17** , 723-732 (2009).

[7] Y.-C. Lo, J.-Y. Fang, Y.-P. Huang, H.-P. D. Shieh, G.-S. Yu, and T. Chiang, “A Novel Patterned Diffuser for High Uniform and High Bright LCD Backlights,” Int. Display Manufactory Con. ’07, 642-645 (2007).

[8] Michael Bass, Eric W. Van Stryland, David R. Williams, William L. Wolfe, *Handbook of Optics, vol. **2***, (McGraw-Hill, New York, 1995).

[9] Francois X. Siilion, and Claude Puech, *Radiosity and Global Illumination*, (Morgan Kaufmann Publishers Inc., San Francisco, 1994).

Chapter 6

Conclusions and Future Works

6.1 Conclusions

Radiometry and photometry have been widely used for various purposes, such as the optical efficiency evaluation, uniformity analysis, and optical property prediction for various optical systems. The studies of the luminair, flat panel display, solar energy, and indoor illumination are assisted by this technology. As the rapid progress of the lighting application, the classification between the light source and object in the triangle in Fig. 1-1 is gradually indeterminate, such as the photo-fluorescent material. The angular modulation and wavelength conversion of this material should be both considered. However, the conventional definitions of radiometry can't completely describe such complicated phenomena.

In this thesis, we study the measurement instruments, mathematical relationships, and calculation methodologies of radiometry for lighting applications. Based on the energy balance equation (Eq. 1.1), the proposed characterization and calculation methodology are verified by practical cases, respectively.

6.1.1 BSDF measurement

For the BTDF measurement, we designed a light source module to produce the collimated beam at various incident angles. Here the collimated beam is produced by a LED combined with a total internal reflection (TIR) lens, and two apertures with 2-mm diameter are used to limit the beam divergent angle within +/- 1 degree. This LED can slide on an arc track to provide variable incident angle θ. The conoscopic

system is used to record the angular spreading function. Through the definition, the BTDF of a scattering film can be recorded and calculated.

6.1.2 Dichromatic BSDF

For the phosphor-converted light-emitting diodes (pcLEDs), the interaction of the illuminating energy with the phosphor would not just behave as a simple wavelength-converting phenomenon, but also a function of various combinations of illumination and viewing geometry. We presents the dichromatic BSDF to characterize the converting and scattering mechanisms of the phosphor layer in the pcLEDs by the measured bidirectional scattering distribution functions (BSDFs). A commercially available pcLED with conformal phosphor coating was used to examine the validity of the proposed model. The close agreement with the measurement illustrates that the proposed characterization opens new perspectives for phosphor-based conversion and scattering feature for white lighting uses.

6.1.3 Energy balance equation calculation

The energy balance equation is an integral formula. We propose a calculation methodology for including the photometric raw data sets into the diffuse illumination design process. The method is based on computing the luminance distribution on the outgoing side of diffusing elements from measured bidirectional scattering distribution functions (BSDFs). The calculation procedure includes the linear superposition and the correcting feedback. As an application example, the method is verified by a commercially available diffusing sheet illuminated by a 32-inch backlighting module. Close agreement (correlation coefficient = 98.6%) with the experimental measurement confirmed the validity of the proposed procedure.

6.1.4 Application - Planar Lighting by Remote Phosphor Sheet

A novel direct-emitting LED backlit for LCDs was demonstrated. Unlike the conventional white LED schemes for display applications, proposed blue light excited planar lighting (BLPL) exploits blue LED chip to remotely excite the YAG-phosphor film and thus render a uniform planar source, where the YAG-phosphor acts as the diffuser film and wavelength down converter simultaneously. Based on the diffusing characterization of YAG-phosphor layer, we examined the optical properties of the BLPL system in viewpoints of uniformity, luminance and mixing capability. Consequently, a prototype 10-mm-thickness BLPL module was demonstrated with 86% uniformity and 9800 nits without using any diffuser film or light guiding plate.

6.2 Future Works

6.2.1 Physical study of BSDF

Although the measurement instruments, mathematical relationships, and calculations have been discussed in this thesis, the physical description of the relationship between the object properties and the BSDF curves should be further studies. These object properties include the surface roughness, refraction index, particle size, geometrical configuration, and so on, which introduce phase changes on the incident wave. The light cannot be treated as being reflected or transmitted only at the interface of materials, but rather the incident light interacts with all the atoms and molecules in the object. As we mentioned in Chapter 2, the BSDF provides a general and useful description of the far-field light distribution. Therefore, we will study on the relation of the physical mechanisms with the BSDF curves.

6.2.1 Polychromatic BSDF

Photo- fluorescent technology have been widely used in many applications,

including cold cathode fluorescent lamp (CCFL) as the most popular light source, pcLED as next generation white light illuminants, and plasma emission devices for information displaying, as Fig. 6-1 shows. In additional to the dichromatic white mixing scheme we proposed, the methodology can be extended to a general form subject to the multiple excitation radiance,

$$\begin{aligned}&\rho(\theta_i,\phi_i,\theta_t,\phi_t)\\&=\rho_{fs}^{\lambda_0-\lambda_0}(\theta_i,\phi_i,\theta_t,\phi_t)+\sum_m(\rho_{fe}^{\lambda_0-\lambda_m}(\theta_i,\phi_i,\theta_t,\phi_t)+\rho_{fs}^{\lambda_m-\lambda_m}(\theta_i,\phi_i,\theta_t,\phi_t)),\end{aligned}\tag{6.1}$$

where λ_0 is the wavelength of the light source, such as the blue light from the GaN LEDs. The index *m* represents *m*-th emitted spectral peak which depends on the light source and the converting properties of the fluorescent material. For instant, the phosphor in a CCFL simultaneously emits the red, green, and blue spectral peaks by the ultraviolet ray excitation. In this case, the multiple excitations of the three spectral peaks can be modeled by the polychromatic BSDF for various configuration designs [1].

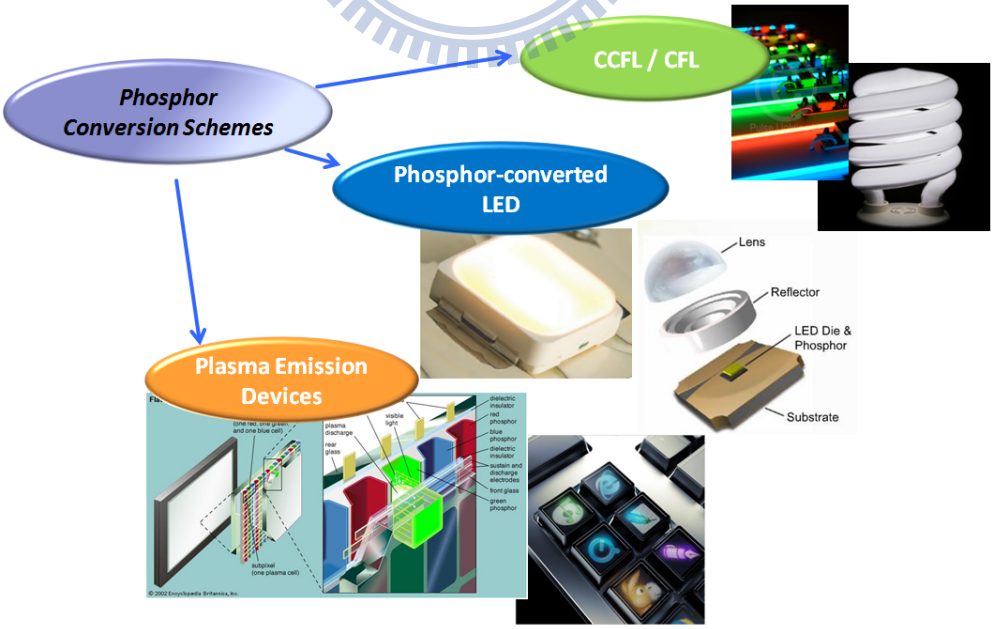

Fig. 6-1 the applications of phosphor conversion schemes

6.2.2 Application – Dual Side Backlighting by Remote Phosphor Sheet

Dual-side displays are suitable for the public information display (PID) application. Due to the high uniformity of the planer lighting with remote phosphor sheet [2], the dual-side backlighting can be realized by the remote phosphor concept. As the configuration proposed in Fig. 6-2, the remote phosphor sheets and free-form surface reflectors for precise light distribution control [3] are expected to perform dual-side planar lighting with uniform brightness and compact structure. The proposed measurement instrument, characterization, and calculation methodology are expected to assist the structure optimization.

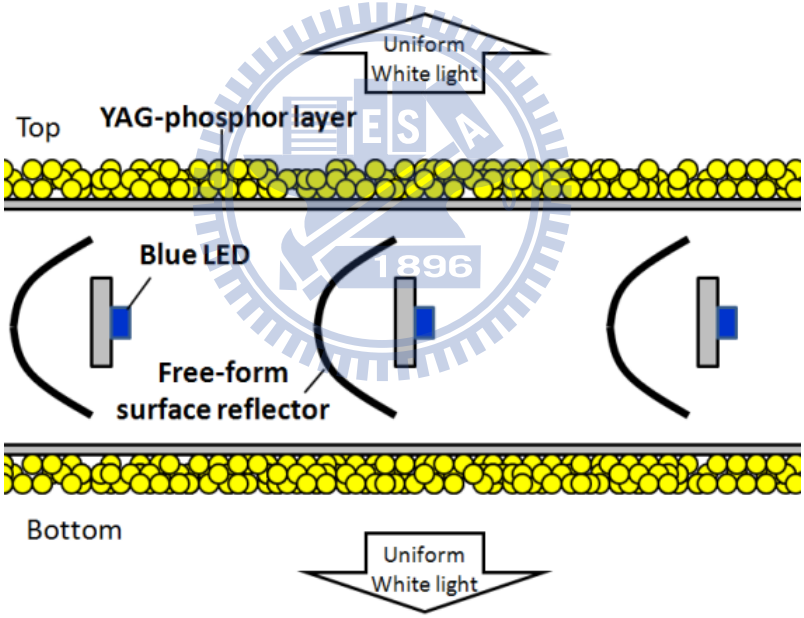

Fig. 6-2 Cross-section of proposed backlight of dual-side display.

6.3 References

[1] Hsin-Tao Huang et al, “UV Excited Flat Lighting (UFL) System for LCD-TV Backlight Application”, SID Int. Symp. Digest Tech. Papers 57.1 (2008).

[2] Bo-Wen Xiao et al, “Optical Properties of Visible-light Excited Phosphor Sheet (VEPS) System,” SID Int. Symp. Digest Tech. Papers 68.4 (2009).

[3] Hao-Wen Chuang et al, “Front Lighting Design for Reflective Display: Free-form Surface Reflector for Uniform Illumination,” Proc. of International Display Manufacturing Conference (IDMC’09)

Appendix

Colorimetry

Colorimetry is the science relating color comparison and matching. As mentioned in **Chapter 1**, for visible light, the optical radiations within wavelengths ranging from 380 nm to 780 nm, the photometric quantities have provided measures to describe the amount of energy. However, in human visual system, the optical radiations arouse not only intensity response (brightness) but also chromatic response (chromaticity). Therefore, in this thesis, colorimetry is imported to specify the chromatic performance of backlight units. The CIEXYZ and CIELUV color spaces, which have been developed for denoting colors numerically, are described in the following paragraphs.

A.1 CIEXYZ

The CIE XYZ system, created by the International Commission on Illuminance (CIE) in 1931, is one of the first mathematically defined color systems that specify colors numerically [1]. The human eye has receptors for short (S), middle (M), and long (L) wavelengths. Thus in principle, three parameters describe a color sensation. The tristimulus values of a color are the amounts of three primary colors in a three-component additive color model needed to match that test color[2]. In the CIE XYZ system, the tristimulus values are called X, Y, and Z. The tristimulus values for a color with a stimulus $\Psi(\lambda)$ can be derived from the color matching functions, the numerical description of the chromatic response of standard observer [3] (see Fig. A-1), according to the following equations:

$$X = k\int_{vis} \Psi(\lambda)\bar{x}(\lambda)d\lambda \tag{A.1}$$

$$Y = k\int_{vis} \Psi(\lambda)\bar{y}(\lambda)d\lambda \tag{A.2}$$

$$Z = k\int_{vis} \Psi(\lambda)\bar{z}(\lambda)d\lambda \tag{A.3}$$

where k is a constant and the integral is taken in the visible light wavelength. The $\bar{y}(\lambda)$ is set so that is identical to the spectral luminous efficiency function $V(\lambda)$ mentioned earlier. Thus the tristimulus value Y directly expresses a photometric quantity.

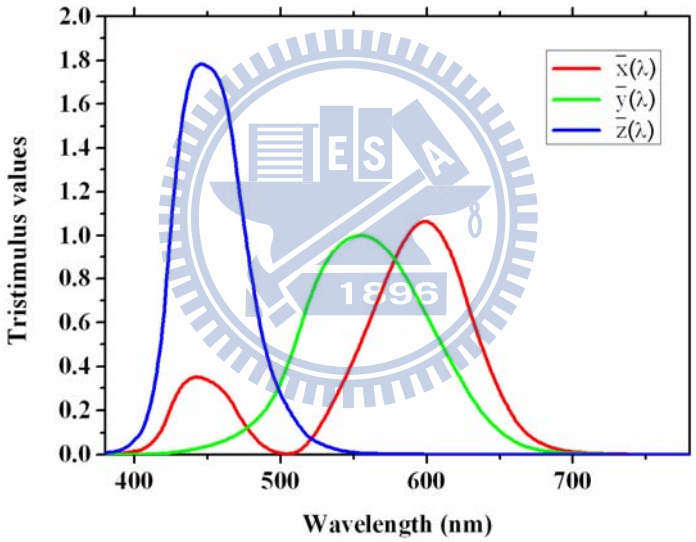

Fig. A-1 Color matching functions $\bar{x}(\lambda)$, $\bar{y}(\lambda)$, and $\bar{z}(\lambda)$ in the CIE XYZ color system.

Basing on CIE XYZ system, a color could be specified by utilizing the tristimulus values *X*, *Y*, and *Z* in a three-dimensional color space, called CIEXYZ color space. Besides, for convenient descriptions of colors, a color space specified by *x*, *y*, and *Y*, known as CIExyY color space, was derived[4]. The *x* and *y* are defined as following equations:

$$x = \frac{X}{X + Y + Z} \tag{A.4}$$

$$y = \frac{Y}{X + Y + Z} \tag{A.5}$$

$$z = \frac{Z}{X + Y + Z} = 1 - x - y \tag{A.6}$$

The z coordinate could be omitted by providing Y parameters which is a measure of the luminance of a color. Accordingly, the chromaticity description of a color could be expressed more conveniently in a two-dimensional plane, which is called CIE xy chromaticity diagram and be widely used in practice (see Fig. A-2).

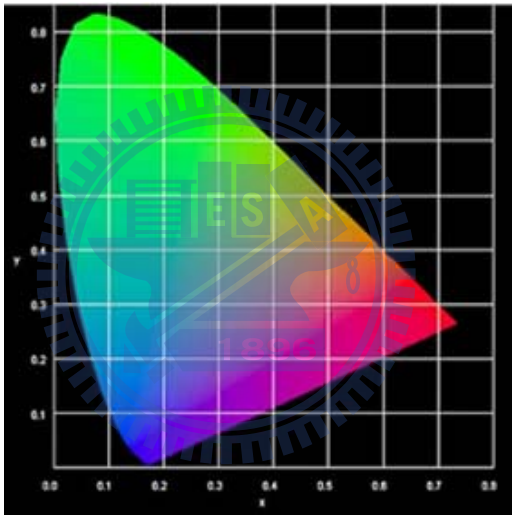

Fig. A-2 xy chromaticity diagram of CIE XYZ color system.

However, the xy chromaticity diagram is highly non-uniform and has been found to be a serious problem in practice [5]. The color difference between two colors could not be calculated by using CIEXYZ color space or xy chromaticity diagram. Therefore, a uniform color space, the CIELUV color space, is proposed to replace the non-uniform CIEXYZ color space.

A.2 CIELUV

The CIELUV color space adopted by CIE in 1976 is an attempt to define an encoding with uniformity in the perceptibility of color difference [6]. Such a uniform color space is based on a simple-to-compute transformation of the 1931 CIEXYZ color space[7,8]. For the non-linear relations from CIEXYZ color space to CIELUV color space, the three-dimensinal orthogonal coordinates adopted in CIELUV color space are defined as follows[9]:

$$L^* = 116(Y / Y_n)^{1/3} - 16 \tag{A.7}$$

$$u^* = 13L^*(u' - u_n') \tag{A.8}$$

$$v^* = 13L^*(v' - v_n') \tag{A.9}$$

where *u'* and *v'* is the coordinates of two-dimensional *u'v'* chromaticity diagram (Fig. A-3) defined as Eq. A.10 and A.11, Y_n, u_n', and v_n' are the tristimulus value and the chromaticity coordinates *u'* and *v'* of reference white, respectively.

$$u' = \frac{4X}{4X + 15Y + 3Z} \tag{A.10}$$

$$v' = \frac{9Y}{X + 15Y + 3Z} \tag{A.11}$$

Basing on the uniform CIELUV color space, the color difference of two colors could be calculated. The color difference $\Delta u'v'$ between two colors (u_1',v_1') and (u_2',v_2') at the *u'v'* chromaticity diagram is defined as[10]:

$$\Delta u'v' = \sqrt{(\Delta u')^2 + (\Delta v')^2} = \sqrt{(u_1' - u_2')^2 + (v_1' - v_2')^2}. \tag{A.12}$$

In this thesis, Eq. A.12 is imported to judge the chromatic performance of the backlight units.

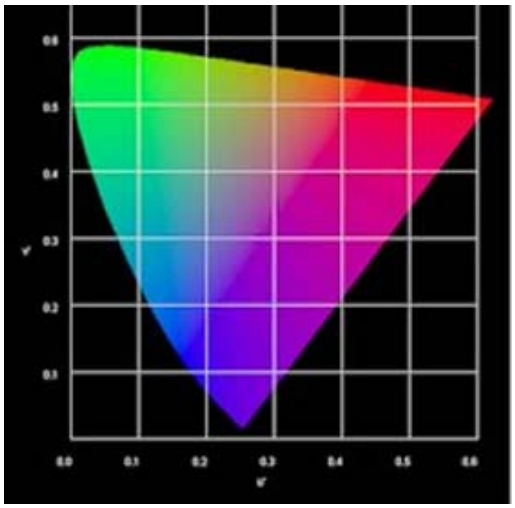

Fig. A-3 *u'v'* chromaticity diagram of the CIELUV color system.

A.3 Color Temperature and Correlated Color Temperature

Color temperature expresses the chromaticity of a given radiation by the temperature of the black body having the same chromaticity as that of the radiation. For radiation whose chromaticity is not exactly equal to that of a black body, correlated color temperature (CCT) is defined as the temperature of the black body whose chromaticity is nearest to that of the radiation. The absolute temperature scale (in kelvin) is used for describing these temperatures. However, it does not necessarily indicate that the light source itself is heated to this temperature. The line connecting the chromaticity points of the series of absolute temperatures of black bodies is called the Plankian locus. For chromaticity not on the Planckian locus, the correlated color temperature can be obtained on the CIE 1960 *uv* chromaticity diagram by drawing a line from the chromaticity point of the radiation in such a manner that it crosses the Planckian locus at a right angle, and determining the temperature corresponding to the cross point. These lines, which are called isotemperature lines, can be obtained for a series of correlated color temperatures and converted into *xy* coordinates. The results are shown in Fig. A-4.

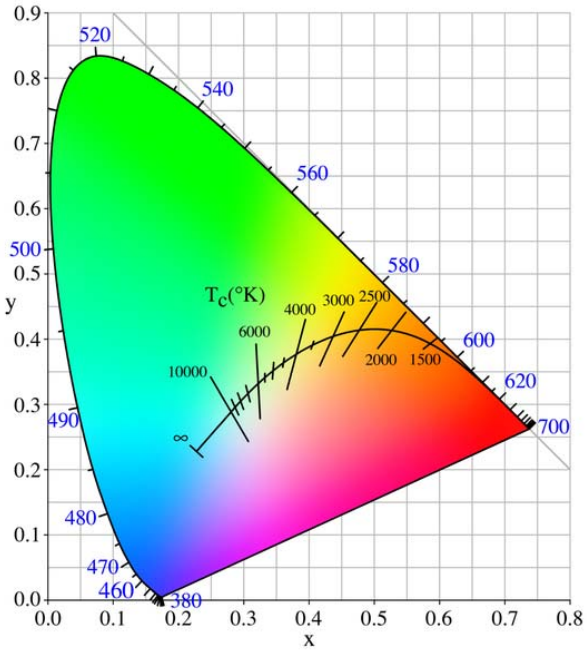

Fig. A-4 Planckian locus and iso-temperature lines.

A.4 Reference

[1] T. Smith and J. Guild, "The C.I.E. Colorimetric Standards and Their Use," Transactions of the Optical Society 33 (3), pp. 73-134 (1931)

[2] R. W. Hunt, *Measuring Colour, 3rd Edition*, Fountain Press, England, pp. 39-57 (1998)

[3] A. C. Harris and I. L. Weatherall, "Objective Evaluation of Colour Variation in the Sand-burrowing Beetle Chaerodes Trachyscelides White by Instrumental Determination of CIELAB Values," Journal of the Royal Society of New Zealand, 20(3) (1990)

[4] N. Ohta and A. R. Robertson, *Colorimetry: Fundamentals and Applications*, John Wiley & Sons, pp.76 (2005)

[5] N. Ohta and A. R. Robertson, *Colorimetry: Fundamentals and Applications*, John Wiley & Sons, pp.115 (2005)

[6] N. Ohta and A. R. Robertson, *Colorimetry: Fundamentals and Applications*, John Wiley & Sons, pp.119 (2005)

[7] M. D. Fairchild, *Color Appearance Models*, Reading, Massachusetts, Addison-Wesley (1998)

[8] D. H. Alman, R. S. Berns, G. D. Snyder, and W. A. Larson, “Performance Testing of Color Difference Metrics Using a Color-Tolerance Dataset,” Color Research and Application, vol. **21**, pp.174-188 (1989)

[9] J. Schanda, *Colorimetry: Understanding the CIE System*, Wiley Interscience, pp. 61-64 (2007)

[10] TCO'06 Media Displays, http://www.tcodevelopment.com/, (2006)

Vita

Name: 洪健翔
Birthday: Jan. 19 1982
Address: 台北市內湖路二段 103 巷 100 弄 11 號五樓

Education:

Sep. 06' – Jun. 10': National Chiao Tung University, Hsinchu, Taiwan.
Ph. D. in Institute of Electro-Optical Engineering.

Sep. 04' – Jun. 06': National Chiao Tung University, Hsinchu, Taiwan.
Master in Display Institute.

Sep. 00' – Jun. 04': National Sun Yat-sen University, Kaohsiung, Taiwan.
Bachelor in Physics.

Experience:

Sep. 06' – Jan. 07': Short-term visiting student at Industrial Technology Research Institute.

Dec. 09' – May 10': Intern at Advanced Optoelectronic Technology, Inc.

Publications

Journal Papers

1. Chung-Hao Tien, ***Chien-Hsiang Hung***, and Chi-Hung Lee "Aberrations Measurement of Fiber-End Microlens by Free-Space Microoptical Ronchi Interferometer", *IEEE Photon. Tech. Let.*, vol. 18, no. 16, pp.1768-1770, 2006.
2. Chung-Hao Tien and ***Chien-Hsiang Hung,*** "Micromachined Polarization Beam Splitter with Adjustable Leak Ratio for Optical Pickup," *IEEE Photon. Tech. Let.*, vol. 19, no. 15, pp.1109-1111, 2007.
3. Chung-Hao Tien and ***Chien-Hsiang Hung***, "An iterative model of diffuse illumination from bidirectional photometric data," *Optics Express*, vol. 17, no. 2, pp. 723-732, 2009.
4. Chung-Hao Tien and ***Chien-Hsiang Hung***, "Microlens Arrays by Direct Write Ink-Jet Printing for LCD Backlighting Applications," *IEEE/OSA J. Display Technology*, vol. 5, no. 5, pp. 147-151, 2009.
5. ***Chien-Hsiang Hung*** and Chung-Hao Tien, "Phosphor-converted LED Modeling by Bidirectional Photometric Data," *Optics Express*, vol. 18, no.103, pp. A261-A271, 2010.

International Conference Papers

1. Hsin-Tao Huang, ***Chien-Hsiang Hung***, Yi-Pai Huang, Chung-Hao Tien, C. C. Tsai, Han-Ping D. Shieh, "UV Excited Flat Lighting (UFL) System for LCD-TV Backlight Application," *SID Symposium Digest Tech Papers*, vol. 39, No.57.1, 2008.
2. ***Chien-Hsiang Hung,*** Tsung-Han Yu, Jung-An Cheng, Chi-Hsien Chang, Yi-Hau Hsiau, Chung-Hao Tien, "Microlens Array by Ink-Jet Technology for LCD Backlight Applications," *SID Symposium Digest Tech Papers*, vol. 39, No.P-97, 2008.
3. Bo-Wen Xiao, ***Chien-Hsiang Hung***, Hsin-Tao Huang, Yi-Pai Huang, Chung-Hao Tien, Chuang-Chuang Tsai, and Han-Ping D. Shieh, "Optical Properties of Visible-light Excited Phosphor Sheet (VEPS) System," *SID Symposium Digest Tech Papers*, No.68.4, 2009.
4. ***Chien-Hsiang Hung***, Chung-Hao Tien, "Modeling Diffuse Components by Bidirectional Scatter Distribution Function for LCD Applications," *SID Symposium Digest Tech Papers*, No.36.4, 2009.
5. Bo-Wen Xiao, ***Chien-Hsiang Hung***, Hsin-Tao Huang, Jerry Cheng, Yi-Pai Huang, Chung-Hao Tien, Chuang-Chuang Tsai, and Han-Ping D. Shieh,

"Optical Simulation and Analysis of Visible-light Excited Phosphor Sheet (VEPS) System," Intl. Display Manufacturing Conference 2009. (Distinguished Paper Award)

6. Chung-Hao Tien, ***Chien-Hsiang Hung*** , Bo-Wen Xiao, Hsin-Tao Huang, Yi-Pai Huang, and Chuang-Chuang Tsai, "Planar Lighting by Blue LEDs Array with Remote Phosphor," *Proc. SPIE*, Vol. **7617**, 761707, 2010**.**
7. ***Chien-Hsiang Hung***, Chung-Hao Tien, "Phosphor Modeling of Phosphor Converted LEDs," *SID Symposium Digest Tech Papers*, No.59.3, 2010.

Other Publications

1. ***洪健翔***、黃信道、蕭博文、林姚順、黃乙白、田仲豪, "大尺寸超薄背光模組技術-紫外線激發平面光在液晶顯示器的應用," 化合物半導體與光電技術, 民國97年11月.
2. 鄭榮安、***洪健翔***、謝漢萍, "噴墨列印技術在顯示器元件製程上之應用," 化合物半導體與光電技術, 民國98年1月.

Awards

1. 96學年度國立交通大學光電工程系博士生獎學金
2. 97年度交大華映產學合作優秀獎
3. IDMC'09 Distinguished Paper Award